

1

2

3

## **Automatic tracking of mouse social posture dynamics**

4

## **by 3D videography, deep learning and GPU-accelerated robust optimization**

5

6

**Christian L. Ebbesen<sup>1,2,\*</sup> & Robert C. Froemke<sup>1,2,3,\*</sup>**

7

8 <sup>1</sup> Skirball Institute of Biomolecular Medicine, Neuroscience Institute, Departments of Otolaryngology,

9 Neuroscience and Physiology, New York University School of Medicine, New York, NY, 10016, USA.

10 <sup>2</sup> Center for Neural Science, New York University, New York, NY, 10003, USA.

11 <sup>3</sup> Howard Hughes Medical Institute Faculty Scholar.

12 \* Correspondence to: C.L.E. ([christian.ebbesen@nyumc.org](mailto:christian.ebbesen@nyumc.org)) or R.C.F. ([robert.froemke@med.nyu.edu](mailto:robert.froemke@med.nyu.edu))

## 13 **ABSTRACT**

14 Social interactions powerfully impact both the brain and the body, but high-resolution descriptions of these  
15 important physical interactions are lacking. Currently, most studies of social behavior rely on labor-intensive  
16 methods such as manual annotation of individual video frames. These methods are susceptible to experimenter  
17 bias and have limited throughput. To understand the neural circuits underlying social behavior, scalable and  
18 objective tracking methods are needed. We present a hardware/software system that combines 3D videography,  
19 deep learning, physical modeling and GPU-accelerated robust optimization. Our system is capable of fully  
20 automatic multi-animal tracking during naturalistic social interactions and allows for simultaneous electro-  
21 physiological recordings. We capture the posture dynamics of multiple unmarked mice with high spatial (~2  
22 mm) and temporal precision (60 frames/s). This method is based on inexpensive consumer cameras and is  
23 implemented in python, making our method cheap and straightforward to adopt and customize for studies of  
24 neurobiology and animal behavior.

## 25 INTRODUCTION

26 Objective quantification of natural social interactions is difficult. The majority of our knowledge about animal  
27 social behavior comes from hand-annotation of videos, yielding ethograms of discrete social behaviors such  
28 as ‘social following’, ‘mounting’, or ‘anogenital sniffing’<sup>1</sup>. It is widely appreciated that these methods are  
29 susceptible to experimenter bias and have limited throughput. There is an additional problem with these ap-  
30 proaches, in that manual annotation of video frames yields no detailed information about movement kinemat-  
31 ics and physical body postures. This shortcoming is especially critical for studies relating neural activity pat-  
32 terns or other physiological signals to social behavior. For example, neural activity in many areas of the cer-  
33 ebral cortex are strongly modulated by movement and posture<sup>2,3</sup>, and activity profiles in somatosensory re-  
34 gions can be difficult to analyze without understanding the physics and high-resolution dynamics of touch.  
35 Important aspects of social behavior, from gestures to light touch and momentary glances can be transient and  
36 challenging to observe in most settings, but critical to capturing the details and changes to social relationships  
37 and networks<sup>4,5</sup>. Together the potential for false positives and false negatives can be high, and to date these  
38 issues have thwarted our understanding of the neural basis of somatic physiology and social behavior.

39  
40 The use of deep convolutional networks to recognize objects in images has revolutionized computer vision,  
41 and consequently, also led to major advances in behavioral analysis. Drawing upon these methodological  
42 advances, several recent publications have developed algorithms for tracking, such as ‘DeepLabCut’<sup>6</sup>,  
43 ‘(S)LEAP’<sup>7</sup> and ‘DeepPoseKit’<sup>8</sup>. These methods function by detection of key-points in 2D videos, and esti-  
44 mation of 3D postures is not straightforward in interacting animals<sup>9</sup>. Spatiotemporal regularization is needed  
45 to ensure that tracking is stable and error-free, even when multiple animals are closely interacting. During  
46 mounting or allo-grooming, for example, interacting animals block each other from the camera view and  
47 tracking algorithms can fail. Having a large number of cameras film the animals from all sides can solve these

48 problems<sup>9,10</sup>, but this has required extensive financial resources for equipment, laboratory space and pro-  
49 cessing power, which renders widespread use infeasible.

50

51 In parallel, other studies have used depth-cameras for animal tracking, fitting a physical body-model of the  
52 animal to 3D data<sup>11,12</sup>. These methods are powerful because they explicitly model the 3D movement and poses  
53 of multiple animals. However, due to technical limitations of depth imaging hardware (frame rate, resolution,  
54 motion blur), it is to date only possible to extract partial posture information about small and fast-moving  
55 animals, such as lab mice. Consequently, when applied to mice, these methods are prone to tracking mistakes  
56 when interacting animals get close to each other and the tracking algorithms require continuous manual su-  
57 pervision to detect and correct errors. This severely restricts throughput, making tracking across long time  
58 scales infeasible.

59

60 Here we describe a novel system for multi-animal tracking that combines ideal features from both approaches.  
61 Our method fuses physical modeling of depth data and deep learning-based analysis of synchronized color  
62 video to estimate the body postures, enabling us to reliably track multiple mice during naturalistic social  
63 interactions. Our method is fully automatic (i.e., quantitative, scalable, and free of experimenter bias), is based  
64 on inexpensive consumer cameras, and is implemented in Python, a simple and widely used computing lan-  
65 guage. Together, this makes our method inexpensive to adopt and easy to use and customize, paving a way  
66 for more widespread study of naturalistic social behavior in neuroscience and experimental biomedicine.

## 67 **RESULTS**

### 68 *Raw data acquisition*

69 We established an experimental setup that allowed us to capture synchronized color images and depth images  
70 from multiple angles, while simultaneously recording synchronized neural data (**Fig. 1a**). We used inexpen-  
71 sive, state-of-the-art ‘depth cameras’ for computer vision and robotics. These cameras contain several imaging  
72 modules: one color sensor, two infrared sensors and an infrared laser projector (**Fig. 1b**). Imaging data pipe-  
73 lines, as well as intrinsic and extrinsic sensor calibration parameters can be accessed over USB through a  
74 C/C++ SDK with Python bindings. We placed four depth cameras, as well as four synchronization LEDs  
75 around a transparent acrylic cylinder which served as our behavioral arena (**Fig. 1c**).

76

77 Each depth camera projects a static dot pattern across the imaged scene, adding texture in the infrared spec-  
78 trum to reflective surfaces (**Fig. 1d**). By imaging this highly-textured surface simultaneously with two infrared  
79 sensors per depth camera, it is possible to estimate the distance of each pixel in the infrared image to the depth  
80 camera by stereopsis (by locally estimating the binocular disparity between the textured images). Since the  
81 dot pattern is static and only serves to add texture, multiple cameras do not interfere with each other and it is  
82 possible to image the same scene from multiple angles. This is one key aspect of our method, not possible  
83 with depth imaging systems that rely on actively modulated light (such as the Microsoft Kinect system and  
84 earlier versions of the Intel Realsense cameras).

85

86 Since mouse movement is fast<sup>13</sup>, it is vital to minimize motion blur in the infrared images and thus the final  
87 3D data (‘point-cloud’). To this end, our method relies on two key features. First, we use depth cameras where  
88 the infrared sensors have a global shutter (e.g., Intel D435) rather than a rolling shutter (e.g., Intel D415).  
89 Using a global shutter reduces motion blur in individual image frames, but also enables synchronized image  
90 capture across cameras. Without synchronization between cameras, depth images are taken at different times,

91 which adds blur to the composite point-cloud. We set custom firmware configurations in our recording pro-  
92 gram, such that all infrared sensors on all four cameras are hardware-synchronized to each other by TTL-  
93 pulses via custom-built, buffered synchronization cables (**Fig. 1b**).

94

95 We wrote a custom multithreaded Python program with online compression, that allowed us to capture the  
96 following types of raw data from all four cameras simultaneously: 8-bit RGB images (320 x 210 pixels, 60  
97 frames/s), 16-bit depth images (320 x 240 pixels, 60 frames/s) and the 8-bit intensity trace of a blinking LED  
98 (60 samples/s, automatically extracted in real-time from the infrared images). Our program also captures  
99 camera meta-data, such as hardware time-stamps and frame numbers of each image, which allows us to iden-  
100 tify and correct for possible dropped frames. On a standard desktop PC, the recording system had very few  
101 dropped frames and the video recording frame rate and the imaging and USB image transfer pipeline was  
102 stable (**Fig. 1e,f**).

103

#### 104 *Temporal stability and temporal alignment*

105 In order to relate tracked behavioral data to neural recordings, we need precise temporal synchronization.  
106 Digital hardware clocks are generally stable but their internal speed can vary, introducing drift between clocks.  
107 Thus, even though all depth cameras provide hardware timestamps for each acquired image, for long-term  
108 recordings, across behavioral time scales (hours to days), a secondary synchronization method is required.

109

110 For synchronization to neural data, our recording program uses a USB-controlled Arduino microprocessor to  
111 output a train of randomly-spaced voltage pulses during recording. These voltage pulses serve as TTL triggers  
112 for our neural acquisition system (sampled at 30 kHz) and drive LEDs, which are filmed by the depth cameras  
113 (**Fig. 1a**). The cameras sample an automatically detected ROI to sample the LED state at 60 frames/s, inte-  
114 grating across a full infrared frame exposure (**Fig. 1g**). We use a combination of cross-correlation and robust

115 regression to automatically estimate and correct for shift and drift between the depth camera hardware clocks  
116 and the neural data. Since we use random pulse trains for synchronization, alignment is unambiguous and we  
117 can achieve super-frame-rate-precision. In a typical experiment, we estimated that the depth camera time  
118 stamps drifted with  $\sim 49$   $\mu\text{s}/\text{min}$ . We corrected for this drift to yield stable residuals between TTL flips and  
119 depth frame exposures (**Fig. 1h**). Note that the neural acquisition system is not required for synchronization  
120 and for a purely behavioral study, we can run the same LED-based protocol to correct for potential shift and  
121 drift between cameras by choosing one camera as a reference.

122

### 123 *Detection of body key-points by deep learning*

124 We preprocessed the raw image data to extract two types of information for the tracking algorithm: the loca-  
125 tion in 3D in space of body key-points and the 3D point-cloud corresponding to the body surface of the  
126 animals. We used a deep convolutional neural network to detect key-points in the RGB images, and extracted  
127 the 3D point-cloud from the depth images (**Fig. 2a**). For key-point detection (nose, ears, base of tail, and  
128 neural implant for implanted animals), we used a ‘stacked hourglass network’<sup>14</sup>. This type of network archi-  
129 tecture combines residuals across successive upsampling and downsampling steps to generate its output, and  
130 has been successfully applied to human pose estimation<sup>14</sup> and limb tracking in immobilized flies<sup>15</sup> (**Fig. 2b**,  
131 **Supplementary Fig. 1**).

132

133 We used back-propagation to train the network to output four ‘target maps’, each indicating the pseudo-pos-  
134 terior probability of each type of key-point, given the input image. The target maps were generated by manu-  
135 ally labeling the key-points in training frames, followed by down-sampling and convolution with Gaussian  
136 kernels (**Fig. 2c**, ‘target maps’). We selected the training frames using image clustering to avoid redundant  
137 training on very similar frames<sup>8</sup>. The manual key-point labeling can be done with any labeling software. We

138 customized a version of the lightweight, open source labeling GUI from the ‘DeepPoseKit’ package<sup>8</sup> for the  
139 four types of key-points, which we provide as supplementary software (**Supplementary Fig. 2**).

140

141 In order to improve key-point detection, we used two additional strategies. First, we also trained the network  
142 to predict ‘affinity fields’<sup>16</sup>. We used ‘1D’ affinity fields<sup>8</sup>, generated by convolving the path between labeled  
143 body key-points that are anatomically connected in the animal. With our four key-points, we added seven  
144 affinity fields (‘nose-to-ears’, ‘nose-to-tail’, etc.), that together form a skeletal representation of each body  
145 (**Fig. 2c**, ‘affinity fields’). Thus, from three input channels (RGB pixels), the network predicts eleven output  
146 channels (**Fig. 2d**). As the stacked hourglass architecture involves intermediate prediction, which feeds back  
147 into subsequent hourglass blocks (repeated encoding and decoding, **Fig 2b**), prediction of affinity fields feeds  
148 into downstream predictions of body key-points. This leads to improvement of downstream key-point predic-  
149 tions, because the affinity fields give the network access to holistic information about the body. The intuitive  
150 probabilistic interpretation is that instead of simply asking questions about the keypoints (e.g., ‘do these pixels  
151 look like an ear?’), we can increase predictive accuracy by considering the body context (e.g., ‘these pixels  
152 sort of look like an ear, and those pixels sort of look like a nose – but does this path between the pixels also  
153 look like the path from an ear to a nose?’).

154

155 The second optimization approach was image data augmentation during training<sup>17</sup>. Instead of only training  
156 the network on manually-labeled images, we also trained the network on morphed and distorted versions of  
157 the labeled images (**Supplementary Fig. 3**). Training the network on morphed images (e.g., rotated or en-  
158 larged), gives a similar effect to training on a much larger dataset of labeled images, because the network then  
159 learns to predict many artificially generated, slightly different views of the animals. Training the network on  
160 distorted images is thought to reduce overfitting on single pixels and reduce the effect of motion blur<sup>17</sup>.

161



162 Using a training set of 526 images, and by automatically adjusting learning rate during training, the network  
163 was well-trained (plateaued) within one hour of training on a standard desktop computer (**Fig. 2e**), yielding  
164 good predictions of both body key-points and affinity fields (**Fig. 2f**).

165

### 166 *Pre-processing of 3D video*

167 By aligning the color images to the depth images, and aligning the depth images in 3D space, we could assign  
168 three dimensional coordinates to the detected key-points. We pre-processed the depth data to accomplish two  
169 goals. First, we wanted to align the cameras to each other in space, so we could fuse their individual depth  
170 images to one single 3D point-cloud. Second, we wanted to extract only points corresponding to the animals'  
171 body surfaces from this composite point-cloud.

172

173 To align the cameras in space, we filmed the trajectory of a sphere that we moved around the behavioral  
174 arena. We then used a combination of motion filtering, color filtering, smoothing and thresholding to detect  
175 the location of the sphere in the color frame, extracted the partial 3D surface from the aligned depth data,  
176 and used a robust regression method to estimate the center coordinate (**Fig. 3a**). This procedure yielded a  
177 3D trajectory in the reference frame of each camera (**Fig. 3b**) that we could use to robustly estimate the  
178 transformation matrices needed to bring all trajectories into the same frame of reference (**Fig. 3c**). This ro-  
179 bust alignment is a key aspect of our method, as errors can easily be introduced by moving the sphere too  
180 close to a depth camera or out of the field of view during recording (**Fig. 3b,c**, arrow). After alignment, the  
181 median camera-to-camera difference in the estimate of the center coordinate of the 40-mm-diameter sphere  
182 was only 2.6 mm across the entire behavioral arena (**Fig. 3d,e**).

183

184 We used a similar robust regression method to automatically detect the base of the behavioral arena. We  
185 detected planes in composite point-cloud (**Fig. 3f**) and used the location and normal vector, estimated across

186 60 random frames (**Fig. 3g**), to transform the point-cloud such that the base of the behavioral arena laid in the  
187  $xy$ -plane (**Fig. 3h**). To remove imaging artifacts stemming from light reflection and refraction due to the  
188 curved acrylic walls, we automatically detected the location and radius of the acrylic cylinder (**Fig. 3i**). With  
189 the location of both the arena base and the acrylic walls, we used simple logic filtering to remove all points  
190 associated with the base and walls, leaving only points inside the behavioral arena (**Fig. 3j**). Note that if there  
191 is no constraint on laboratory space, an elevated platform can be used as a behavioral arena, eliminating  
192 imaging artifacts associated with the acrylic cylinder.

193

#### 194 *Loss function design*

195 The pre-processing pipeline described above takes color and depth images as inputs, and outputs two types  
196 of data: a point-cloud, corresponding to the surface of the two animals, and the 3D coordinates of detected  
197 body key-points (**Fig. 4a, Supplementary Video 1**). To track the body postures of interacting animals across  
198 space and time, we developed an algorithm that incorporates information from both data types. The basic idea  
199 of the tracking algorithm is that for every frame, we fit the mouse bodies by minimizing a loss function of  
200 both the point-cloud and key-points, subject to a set of spatiotemporal regularizations.

201

202 For the loss function, we made a simple parametric model of the skeleton and body surface of a mouse. The  
203 body model consists of two prolate spheroids (the ‘hip ellipsoid’ and ‘head ellipsoid’), with dimensions based  
204 on an average adult mouse (**Fig. 4b**). The head ellipsoid is rigid, but the hip ellipsoid has a free parameter ( $s$ )  
205 modifying the major and minor axes to allow the hip ellipsoids to be longer and narrower (e.g., during stretch-  
206 ing, running, or rearing) or shorter and wider (e.g., when still or self-grooming). The two ellipsoids are con-  
207 nected by a joint that allows the head ellipsoid to turn left/right and up/down within a cone corresponding to  
208 the physical movement limits of the neck.

209

210 Keeping the number of degrees of freedom low is vital to make loss function minimization computationally  
211 feasible<sup>18</sup>. Due to the rotational symmetry of the ellipsoids, we could choose a parametrization with 8 degrees  
212 of freedom per mouse body: the central coordinate of the hip ellipsoid ( $x, y, z$ ), the rotation of the major axis  
213 of the hip ellipsoid around the  $y$ - and  $z$ -axis ( $\beta, \gamma$ ), the left/right and up/down rotation of the head ellipsoid ( $\theta$ ,  
214  $\varphi$ ), and the stretch of the hip ellipsoids ( $s$ ). For the implanted animal, we added an additional sphere to the  
215 body model, approximating the surface of the head-mounted neural implant (**Fig. 4b**). The sphere is rigidly  
216 attached to the head ellipsoid and has one degree of freedom; a rotational angle ( $\psi$ ) that allows the sphere to  
217 rotate around the head ellipsoid, capturing head tilt of the implanted animal. Thus, in total, the joint pose (the  
218 body poses of both mice) was parametrized by only 17 variables.

219

220 To fit the body model, we adjusted these parameters to minimize a weighted sum of two loss terms: (i) The  
221 shortest distance from every point in the point-cloud to body model surface. (ii) The distance from detected  
222 key-points to their corresponding location on the body model surface (e.g., nose key-points near the tip of one  
223 of the head ellipsoids, tail key-points near the posterior end of a hip ellipsoid).

224

225 We then used several different approaches for optimizing the tracking. First, for each of the thousands of point  
226 in the point-cloud, we needed to calculate the shortest distance to the body model ellipsoids. Calculating these  
227 distances exactly is not computationally feasible, as this requires solving a six-degree polynomial for every  
228 point<sup>19</sup>. As an approximation, we instead used the shortest distance to the surface, along a path that passes  
229 through the centroid (**Supplementary Fig. 4a,b**). Calculating this distance could be implemented as pure  
230 tensor algebra<sup>20</sup>, which could be executed efficiently on a GPU in parallel for all points simultaneously. Sec-  
231 ond, to reduce the effect of imaging artifacts in the color and depth imaging (which can affect both the point-  
232 cloud or the 3D coordinates of the key-points), we clipped distance losses at 3 cm, such that distant ‘outliers’

233 do contribute and not skew the fit (**Supplementary Fig. 4c**). Third, because pixel density in the depth images  
234 depends on the distance from the depth camera, we weighed the contribution of each point in the point-cloud  
235 by the squared distance to the depth camera (**Supplementary Fig. 4d**). Fourth, to ensure that the minimiza-  
236 tion does not converge to unphysical joint postures (e.g., where the mouse bodies are overlapping), we added  
237 a penalty term to the loss function if the body models overlap. Calculating overlap between two ellipsoids is  
238 computationally expensive<sup>21</sup>, so we computed overlaps between implant sphere and spheres centered on the  
239 body ellipsoids with a radius equal to the minor axis (**Supplementary Fig. 4f**). Fifth, to ensure spatiotemporal  
240 continuity of body model estimates, we also added a penalty term to the loss function, penalizing overlap  
241 between the mouse body in the current frame, and other mouse bodies in the previous frame. This ensures  
242 that the bodies do not switch place, something that could otherwise happen if the mice are in joint poses with  
243 certain mirror symmetries (**Supplementary Fig. 4g,h**).

244

#### 245 *GPU-accelerated robust optimization*

246 Minimizing the loss function requires solving three major challenges. The first challenge is computational  
247 speed. The number of key-points and body parts is relatively low (~tens), but the number of points in the  
248 point-cloud is large (~thousands), which makes the loss function computationally expensive. For minimiza-  
249 tion, we need to evaluate the loss function multiple times per frame (at 60 frames/s). If loss function evaluation  
250 is not fast, tracking becomes unusably slow. The second challenge is that the minimizer has to properly ex-  
251 plore the loss landscape within each frame and avoid local minima. In early stages of developing this algo-  
252 rithm, we were only tracking interacting mice with no head implant (**Supplementary Video 2**). In that case,  
253 for the small frame-to-frame changes in body posture, the loss function landscape was nonlinear, but approx-  
254 imately convex, so we could use a fast, derivative-based minimizer to track changes in body posture (geodesic  
255 Levenberg-Marquardt steps<sup>18</sup>). For use in neuroscience experiments, however, one or more mice might carry  
256 a neural implant for recording or stimulation. The implant is generally at a right angle and offset from the

257 ‘hinge’ between the two hip and head ellipsoids, which makes the loss function highly non-convex<sup>22</sup>. The  
258 final challenge is robustness against local minima in state space. Even though a body posture minimizes the  
259 loss in a single frame, it might not be an optimal fit, given the context of other frames (e.g., spatiotemporal  
260 continuity, no unphysical movement of the bodies).

261

262 To solve these three challenges – speed, state space exploration, and spatiotemporal robustness – we designed  
263 a custom GPU-accelerated minimization algorithm, which incorporates ideas from annealed particle filters<sup>23</sup>  
264 and online Bayesian filtering<sup>24</sup>. To maximize computational speed, the algorithm was implemented as pure  
265 tensor algebra in Pytorch, a high-performance GPU computing library<sup>25</sup>. Annealed particle filters are suited  
266 to explore highly non-convex loss surfaces<sup>23</sup>, which allowed us to avoid local minima within each frame.  
267 Between frames, we used online Bayesian filtering, to avoid being trapped in low-probability solutions given  
268 the preceding tracking. For every frame, we first proposed the state of the 17-parameters using kernel-recur-  
269 sive least-squares tracking (‘KRLS-T’<sup>24</sup>) from a Bayesian filter bank based on preceding frames. After particle  
270 filter-based loss function minimization within a single frame, we updated the Bayesian filter bank, and pro-  
271 posed a particle filter starting point for the next frame. This strategy has three major advantages. First, by  
272 proposing a solution, taking into account previous variables and their covariances, we often already started  
273 loss function minimization close to the new minimum. Second, if the Bayesian filter deems that the fit for a  
274 single frame is unlikely, based on the preceding frames, this fit will only weakly update the Bayesian filter  
275 bank, and thus only weakly perturb the upcoming tracking. This gave us a convenient way to balance the  
276 information provided by the fit of a single frame, and the ‘context’ provided by previous frames. Third, the  
277 Bayesian filter-based approach is only dependent on previously tracked frames, not future frames. This is in  
278 contrast to other approaches to incorporating context that rely on versions of backwards belief propaga-  
279 tion<sup>5,15,26</sup>. Since our algorithm only uses past data, it is in principle possible to optimize our algorithm for real-  
280 time use in closed-loop experiments.

281

282 For each frame, we explored the loss surface with 200 particles (**Fig. 4b,c**). We generated the particles by  
283 perturbing the proposed minimum, based on the previous frames, by quasi-random, low-discrepancy sam-  
284 pling<sup>27</sup> (**Supplementary Fig. 5**). We exploited the fact that the loss function structure allowed us to execute  
285 several key steps in parallel, across multiple independent dimensions, and implemented these calculations as  
286 vectorizes tensor operations. This allowed us to leverage the power of CUDA kernels for fast tensor algebra  
287 on the GPU<sup>25</sup>. Specifically, to efficiently calculate the point-cloud loss (shortest distance from a point in the  
288 point-cloud to the surface of a body model), we calculated the distance to all five body model spheroids for  
289 all points in the point-cloud and for all 200 particles, in parallel (**Fig. 4c**). We then applied fast minimization  
290 kernels across the two body models, to generate a smallest distance to either mouse, for all points in the  
291 pointcloud. Because the mouse body models are independent, we only had to apply a minimization kernel to  
292 calculate the smallest distance, for every point, to 40,000 (200 x 200) joint poses if the two mice. These  
293 parallel computation steps are a key aspect of our method, which allows our tracking algorithm to avoid the  
294 ‘curse of dimensionality’, by not exploring a 17-dimensional space, but rather explore the intersection of two  
295 independent 8-dim and 9-dim subspaces in parallel.

296

### 297 *Tracking algorithm performance*

298 To ensure that the tracking algorithm did not get stuck in suboptimal solutions, we forced the particle filter to  
299 explore a large search space within every frame (**Fig. 5a-c**). In successive iterations, we gradually made per-  
300 turbations to the particles smaller and smaller by annealing the filter<sup>23</sup>), to approach the minimum. At the end  
301 of each iteration, we ‘resampled’ the particles by picking the 200 joint poses with the lowest losses in the 200-  
302 by-200 matrix of losses. This resampling strategy has two advantages. First, it can be done without fully  
303 sorting the matrix<sup>28</sup>, the most computationally expensive step in resampling<sup>29</sup>. Second, it provides a kind of  
304 quasi-‘importance sampling’. During resampling, some poses in the next iteration might be duplicates (picked

305 from the same row or column in the 200-by-200 loss matrix.), allowing particles in each subspace to collapse  
306 at different rates (if the particle filter is very certain about one body pose, but not the other, for example).

307

308 By investigating the performance of the particle filter across iterations, we found that the filter generally  
309 converged within five iterations (**Fig. 5d**), providing good tracking across frames (**Fig. 5e**). In every frame,  
310 the particle filter fit yields a noisy estimate of the 3D location of the mouse bodies. The transformation from  
311 the joint pose parameters (e.g., rotation angles, spine scaling) to 3D space is highly nonlinear, so simple  
312 smoothing of the trajectory in pose parameter space would distort the trajectory in real space. Thus, we filtered  
313 the tracked trajectories by a combination of Kalman-filtering and maximum likelihood-based smoothing<sup>30,31</sup>  
314 and 3D rotation smoothing in quaternion space<sup>32</sup> (**Supplementary Fig. 6c-e, Supplementary Video 3**).

315

316 Representing the joint postures of the two animals with this parametrization was highly data efficient, reduc-  
317 ing the memory footprint from ~3.7 GB/min for raw color/depth image data, to ~0.11 GB/min for pre-pro-  
318 cessed point-cloud/key-point data to ~1 MB/min for tracked body model parameters. On a regular desktop  
319 computer with a single GPU, we could do key-point detection in color image data from all four cameras in  
320 ~2x real time (i.e. it took 30 mins to process a 1 hr experimental session). Depth data processing (point-cloud  
321 merging and key-point deprojection) ran at ~0.7x real time, and the tracking algorithm ran at ~0.2x real time  
322 (if the filter uses 200 particles and 5 filter iterations per frame). Thus, for a typical experimental session (~  
323 hours), we would run the tracking algorithm overnight, which is possible because the code is fully unsuper-  
324 vised.

325

326 Note that this version of the algorithm is written for active development, not pure speed. For example, a large  
327 part of the processing time is spent reading/writing data to disk, and – while convenient for modifying and  
328 experimenting with the code – it is not necessary to first process color, then depth and then run a tracking

329 algorithm step, for example. In its present form, the code is fast enough to be useful, but not optimized to the  
330 theoretical maximum speed.

331

### 332 ***Error detection***

333 Error detection and correction is a critical component of behavioral tracking. Even if error rates are nominally  
334 low, errors are non-random, and errors often happen exactly during the behaviors in which we are most inter-  
335 ested: interactions. In multi-animal tracking, two types of tracking error are particularly fatal as they com-  
336 pound over time: identity errors and body orientation errors (**Supplementary Fig. 7a**). In conventional track-  
337 ing approaches using only 2D videos, it is often difficult to correctly track identities when interacting mice  
338 are closely interacting, allo-grooming, or passing over and under each other. Although swapped identities can  
339 be corrected later once the mice are well-separated again, this still leaves individual behavior during the actual  
340 social interaction unresolved<sup>5,26</sup>. We found that our tracking algorithm was robust against both identity swaps  
341 (**Supplementary Fig. 7b-e**) and body direction swaps (**Supplementary Fig. 8**). This observation agrees with  
342 the fact that tracking in three-dimensional space (subject to our implemented spatiotemporal regularizations)  
343 *a priori* ought to allow better identity tracking; In full 3D space it is easier to determine who is rearing over  
344 whom during an interaction, for example.

345

346 To test our algorithm for more subtle errors, we manually inspected 500 frames, randomly selected across an  
347 example 21 minute recording session. In these 500 frames, we detected one tracking mistake, corresponding  
348 to 99.8% correct tracking (**Supplementary Fig. 9a**). The identified tracking mistake was visible as a large,  
349 transient increase in the point-cloud loss function (**Supplementary Fig. 9b**). After the tracking mistake, the  
350 robust particle filter quickly recovered to correct tracking again (**Supplementary Fig. 9c**). By detecting such  
351 loss function anomalies, or by detecting ‘unphysical’ postures or movements in the body models, potential  
352 tracking mistakes can be automatically ‘flagged’ for inspection (**Supplementary Fig. 9c,d**). After inspection,



353 errors can be manually corrected or automatically corrected in many cases, for example by tracking the par-  
354 ticle filter backwards in time after it has recovered. As the algorithm recovers after a tracking mistake, it is  
355 generally unnecessary to actively supervise the algorithm during tracking, and manual inspection for potential  
356 errors can be performed after running the algorithm overnight.

357

### 358 *Automated analysis of movement kinematics and social behavior*

359 Despite the high level of data compression (from raw images to pre-processed data to only 17 dimensions), a  
360 human observer can clearly distinguish social events in the tracked data (**Fig. 5f**). The major motivation be-  
361 hind developing our method, however, was to eschew manual labeling especially for large-scale datasets on  
362 the order of days to months of video tracking of the same animals. As a validation of our tracking method, we  
363 demonstrate that our methods can automatically extract both movement kinematics and behavioral states  
364 (movement patterns, social events) during spontaneous social interactions. Moreover, data generated by our  
365 tracking method are compatible with two types of analyses: (i) Modern data-mining methods for unsupervised  
366 discovery of behavioral states (specifically, state space modeling) and (ii) Template-based analysis, detecting  
367 behaviors of interest based on prior knowledge. Template-based methods are better suited than unsupervised  
368 methods for detecting certain types of behaviors (see Discussion), so it is a major advantage that our data are  
369 amenable to both types of analysis. Both types of analysis are quantitative and fully automatic, solving two  
370 major issues with manual labeling (subjective experimenter bias and limited throughput).

371

372 To demonstrate template-based analysis, we defined social behaviors of interest as templates and matched  
373 these templates to tracked data. We know that anogenital sniffing<sup>33</sup> and nose-to-nose touch<sup>34</sup> are prominent  
374 events in rodent social behavior, so we designed a template to detect these events. In this template, we ex-  
375 ploited the fact that we could easily calculate both body postures and movement kinematics, in the reference  
376 frame of each animal's own body. For every frame, we first extracted the 3D coordinates of the body model

377 skeleton (**Supplementary Fig. 5**). From these skeleton coordinates, we calculated the position (**Fig. 6a**) and  
378 a three-dimensional speed vector for each mouse ('forward speed', along the hip ellipsoid, 'left speed' per-  
379 pendicular the body axis and 'up speed' along the z-axis; **Fig. 6b, Supplementary Fig. 8**). We also calculated  
380 three instantaneous 'social distances', defined as the 3D distance between the tip of each animal's noses  
381 ('nose-to-nose'; **Fig. 6b**), and from the tip of each animal's nose to the posterior end of the conspecific's hip  
382 ellipsoid ('nose-to-tail'; **Fig. 6b**). From these social distances, we could automatically detect when the mouse  
383 bodies were in a nose-to-nose or a nose-to-tail configuration, and in a single 20 min experimental session, we  
384 observed multiple nose-to-nose and nose-to-tail events (**Fig. 6c**). It is straightforward to further subdivide  
385 these social events by body postures and kinematics, to, e.g., separate stationary nose-to-tail configurations  
386 (anogenital sniffing/grooming) and nose-to-tail configurations during locomotion (social following).

387

388 To demonstrate unsupervised behavioral state discovery, we used GPU-accelerated probabilistic program-  
389 ming<sup>35</sup> and state space modeling to automatically detect and label movement states. To discover types loco-  
390 motor behavior, we fitted a 'sticky' multivariate hidden Markov model<sup>36</sup> to the two components of the speed  
391 vector that lie in the  $xy$ -plane (**Supplementary Fig. 9a-h**). With five hidden states, this model yielded inter-  
392 pretable movement patterns that correspond to known mouse locomotor 'syllables': resting (no movement),  
393 turning left and right, and moving forward at slow and fast speeds (**Fig. 6d**). Fitting a similar model with three  
394 hidden states to the z-component of the speed vector (**Supplementary Fig. 9i-n**) yielded interpretable and  
395 known 'rearing syllables': rest, rearing up and ducking down (**Fig. 6e**). Using the maximum a posterior prob-  
396 ability from these fitted models, we could automatically generate locomotor ethograms and rearing ethograms  
397 for the two mice (**Fig. 6b**).

398

399 In line with previous observations, we found that movement bouts were short (medians,  
400 rest/left/right/fwd/ffwd: 0.83/0.50/0.52/0.45/0.68 s, a 'sub-second' timescale<sup>13</sup>). In the locomotion ethograms,

401 bouts of rest were longer than bouts of movement (all  $p < 0.05$ , Mann-Whitney U-test; **Fig. 6f**) and bouts of  
402 fast forward locomotion was longer than other types of locomotion (all  $p < 0.001$ , Mann-Whitney U-test; **Fig.**  
403 **6f**). In the rearing ethograms, the distribution of rests was very wide, consisting of both long (~seconds) and  
404 very short (~tenths of a second) periods of rest (**Fig. 6g**). As expected, by plotting the rearing height against  
405 the duration of rearing syllables, we found that short rests in rearing were associated with standing high on  
406 the hind legs (the mouse rears up, waits for a brief moment before ducking back down), while longer rests  
407 happened when the mouse was on the ground (ation of rearing syllabpearman rank; **Fig. 6h**). Like the move-  
408 ment types and durations, the transition probabilities from the fitted hidden Markov models were also in  
409 agreement with known behavioral patterns. In the locomotion model, for example, the most likely transition  
410 from “rest” was to “slow forward”. From “slow forward”, the mouse was likely to transition to “turning left”,  
411 “fast forward” or “turning right”, it was unlikely to transition directly from “fast forward” to “rest” or from  
412 “turning left” to “turning right, and so on (**Supplementary Fig. 9o,p**).

413

414 Finally, our method recovered the 3D head direction of both animals. The head direction of the implanted  
415 animal was given by the skeleton of the body model (the implant is fixed to the head). As mentioned above,  
416 we exploited the rotational symmetry of the body model of the conspecific to decrease the dimensionality of  
417 the search space during tracking (**Fig. 4c**). However, from the 3D coordinates of the detected key-points, we  
418 could still infer the 3D head direction (**Supplementary Fig. 10**) and it matched known mouse behavior (**Sup-**  
419 **plementary Fig. 11**). This feature is of particular interest to social neuroscience, since – while rodents clearly  
420 respond to the behavior of conspecifics – we are still only beginning to discover how the rodent brain encodes  
421 the gaze direction and body postures of others<sup>37</sup>.

## 422 **DISCUSSION**

423 We combined 3D videography, deep learning and GPU-accelerated robust optimization to estimate the posture  
424 dynamics of multiple freely-moving mice, engaging in naturalistic social interactions. Our method is cost-  
425 effective (requiring only inexpensive consumer depth cameras and a GPU), has high spatiotemporal precision,  
426 is compatible with neural implants for continuous electrophysiological recordings, and tracks unmarked ani-  
427 mals of the same coat color (e.g., enabling behavioral studies in transgenic mice). Our method is fully unsu-  
428 pervised, which makes the method scalable across multiple PCs or GPUs. Unsupervised tracking allows us to  
429 investigate social behavior across long behavioral time scales – beyond what is feasible with manual annota-  
430 tion – to elucidate developmental trajectories, dynamics of social learning, or individual differences among  
431 animals<sup>38,39</sup>, among other types of questions. Finally, our method uses no message-passing from future frames,  
432 but only relies on past data, which makes the method a promising starting point for real-time tracking.

433

### 434 ***Reasons to study naturalistic social interactions in 3D***

435 Social dysfunctions can be devastating symptoms in a multitude of mental conditions, including autism spec-  
436 trum disorders, social anxiety, depression, and personality disorders<sup>40</sup>. Social interactions also powerfully  
437 impact somatic physiology, and social interactions are emerging as a promising protective and therapeutic  
438 element in somatic conditions, such as inflammation<sup>41</sup> and chronic pain<sup>42</sup>. These disorders have high incidence  
439 but generally lack effective treatment options, largely because even the neurobiological basis of ‘healthy’  
440 social behavior is poorly understood.

441

442 In neuroscience and experimental biomedicine, there has been major technical progress in recording tech-  
443 niques for freely moving animals, with high-density electrodes<sup>43,44</sup>, and head-mounted multi-photon micro-  
444 scopes<sup>45,46</sup>. Moreover, newer methods are being developed for tracking complex patterns of animal behav-

445 ior<sup>47,48</sup>. Here we provide a new method to complement these approaches for feasible, quantitative, and auto-  
446 mated behavioral analysis. A major next step for future work is to apply such algorithms to animal behavior  
447 in different conditions. For example, the algorithm can easily be adapted to track other animal body shapes  
448 such as juvenile mice or other species, or movable, deformable objects that might be important for foraging  
449 or other behaviors in complex environments.

450

#### 451 ***What is the advantage of a body model?***

452 In automated analysis of behavioral states, there are three main approaches: nonlinear clustering<sup>7,49–55</sup>,  
453 probabilistic state space modeling<sup>13,56–59</sup> and template matching<sup>5,11,26</sup>. In nonlinear clustering, tracked body  
454 coordinates (and derived quantities, such as time derivatives or spectral components) are segmented into dis-  
455 crete behaviors by density-based clustering, typically after nonlinear projection down to a low-dimensional  
456 2D space<sup>7,49–53,55</sup> or 3D space<sup>60</sup>. Density-based clusters are manually inspected and curated, such that clusters  
457 judged as similar are merged and clusters are assigned names (e.g., ‘locomotion’, ‘grooming’, etc.). This  
458 approach is simple and robust, but still flexible enough to discover behavioral changes due to interactions  
459 with conspecifics<sup>52,53</sup>. A limitation of this approach, however, is that nonlinear clustering directly on the  
460 tracked kinematic features does not allow explicit modeling of history dependence or hierarchical structure.

461

462 In principle, state space models are highly expressive, allowing for complex nested structures of hidden states,  
463 observational models, covariance structures and temporal dependencies, e.g., autoregressive terms<sup>13</sup>, linear  
464 dynamics<sup>61</sup>, and hierarchies<sup>39</sup>. In practice, however, state space models are not easily fit to data. Complex  
465 models quickly become prohibitively computationally expensive and approximate fitting strategies, such as  
466 variational inference, show poor convergence for complex models<sup>62</sup>. Finally, and most importantly, model  
467 comparison is still an unsolved problem and methods guaranteed to discover a ‘true’ latent structure from data  
468 (e.g., number of states or transition graph structure) do not exist<sup>36,63</sup>.

469

470 Neither state space modeling nor nonlinear clustering requires an explicit body model of the animal. In prin-  
471 ciple, any tracked points on the body can be used, as long as their statistics differ enough between distinct  
472 behaviors that they still form significantly different clusters. What is the advantage of an actual body model?  
473 First, even though in principle, any tracked points on an animal can be used for unsupervised behavioral  
474 analysis – body posture features based on the actual body geometry are often both more powerful and more  
475 interpretable in practice<sup>64</sup>. For example, a body model lets us specify appropriate generative models for state  
476 space modeling. Specifying appropriate probability distributions over variables with unknown densities and  
477 covariances is not straightforward, but specifying priors over the parameters of an understandable body model  
478 with known physical constraints is an advantage for this type of analysis.

479

480 Second, unsupervised methods are not well-suited for the discovery of behaviors that happen rarely or are  
481 kinematically similar to other behaviors. In order for rare or kindred behaviors to form identifiable clusters,  
482 it may be necessary to collect extremely large datasets, beyond what is realistic to collect in typical neurosci-  
483 ence experiments, and beyond what it is computationally feasible to analyze. These complications get even  
484 worse when considering the joint statistics of multiple animals. A physical model of the bodies allows us to  
485 overcome these problems by simple template matching and we can easily specify templates that flag social  
486 poses (nose-to-nose and nose-to-tail touch, in our example). Moreover, of particular interest to neural record-  
487 ings, a body model lets us regress out proprioceptive and movement-related signals, known to align to an  
488 egocentric, body-centered reference frame<sup>3,65–67</sup>.

489

490 ***The tracking algorithm is easy to update***

491 Our data acquisition pipeline and tracking algorithm is open source and implemented in Python, a widely  
492 used programming language in machine learning. This makes it easy to update the algorithm with methodo-  
493 logical advances in the field. Deep learning in 3D is still thought to be in its infancy<sup>68</sup>, but along with technical  
494 developments in depth imaging hardware (for video games, self-driving cars and other industrial applications),  
495 there are exciting developments in analysis, including deep learning methods for detection of deformable ob-  
496 jects from image<sup>69-71</sup> and point-cloud<sup>72,73</sup> data, geometric and graph-based tricks for GPU-accelerated analysis  
497 of 3D data<sup>74-76</sup>, and methods for physical modeling of deformable bodies<sup>77-79</sup>.

498

499 Our pre-processing pipeline generates a highly compressed data representation, consisting of a 3D point-cloud  
500 and key-points, sampled at 60 fps. Storing and sharing the raw depth and color video frames from multiple  
501 cameras, across long behavioral time scales (hours to days) is not feasible, but storing and sharing the com-  
502 pressed, pre-processed data format is possible. This is a major advantage for two reasons. First, as deep learn-  
503 ing methods for 3D data improve, old datasets can be re-analyzed and mined for new insights. Second, abun-  
504 dantly available 3D datasets of animal behavior let machine learning researchers test and benchmark new  
505 methods on experimental data. This enables a development cycle for improving behavioral analysis, by which  
506 adoption of 3D-videography-based behavioral tracking in biology can contribute positively to future method-  
507 ological developments in the machine learning community.

508

509 ***Moving towards real-time tracking***

510 Our algorithm is unsupervised, does not use any message-passing from future frames, and robustly recovers  
511 from tracking mistakes. Since the algorithm relies purely on past data, it is in principle possible to run the  
512 algorithm in real-time. Currently, the processing time per frame is higher than the camera frame rate (60  
513 frames/s). However, our algorithm is not fully optimized and there are multiple speed improvements, which

514 are straightforward to implement. For example, in the current version of the algorithm, we first record the  
515 images to disk, and then read and pre-process the images later. This is convenient for algorithm development  
516 and exploration, but writing and reading the images to disk, and moving them onto and off a GPU are time-  
517 intensive steps. During pre-processing, it is possible to increase the speed and precision of key-point detection  
518 by implementing peak detection as a convolutional layer<sup>8</sup> and it may be possible to perform key-point detec-  
519 tion directly on the 1-channel infrared images instead of the 3-channel color images. Grayscale infrared im-  
520 ages are faster to process and we would be able to perform experiments in visual darkness, which is less  
521 stressful and more appropriate for nocturnal mice. As shown in **Figure 1d**, the infrared images are ‘contami-  
522 nated’ with a dotted grid of points from the infrared laser projector, but – as evidenced by the usefulness of  
523 pixel dropout in image data augmentation<sup>17</sup> (**Supplementary Fig. 3**) – it should be possible to train a network  
524 to ‘disregard’ the dotted grid during key-point detection. We may also be able to reduce the number of required  
525 particle filtering steps between frames. For example, we could force a network to learn to draw particle sam-  
526 ples more intelligently, based on learned covariance patterns in natural mouse movement. Additionally, we  
527 could try to combine our particle filter with gradient-based optimization methods (start with a particle filter  
528 step to search for loss function basins and then use fast, parallel Levenberg-Marquardt steps<sup>18</sup> to quickly move  
529 particles to the bottom of the basins, for example).

530

531 Beyond these optimizations, tracking at a lower frame rate would allow more data processing time per frame.  
532 Our robust, particle-filter-based tracker with online forecasting is an ideal candidate for this task. Going for-  
533 ward, we will investigate the performance of the algorithm at lower frame rates and explore ways to increase  
534 tracking robustness further, by implementing other recently described tracking algorithm tricks, such as using  
535 the optical flow between video frames to link key-points together in multi-animal tracking (‘SLEAP’<sup>7,80</sup>),  
536 real-time painting-in of depth artifacts<sup>81</sup> and even better online trajectory forecasting, for example using deep



537 Gaussian processes<sup>82</sup> or a neural network trained to propose trajectories based on mouse behavior. Experi-  
538 mentation and optimization is clearly needed, but our fully unsupervised algorithm – requiring data transfer  
539 from only a few cameras, with deep convolutional networks, physical modeling and particle filter tracking  
540 implemented as tensor algebra on the same GPU – is a promising starting point for the development of real-  
541 time, multi-animal 3D tracking.

## 542 REFERENCES

- 543 1. Crusio, W. E., Sluyter, F. & Gerlai, R. T. Ethogram of the mouse. in *Behavioral Genetics of the*  
544 *Mouse* 17–22 (Cambridge University Press, 2013). doi:10.1017/CBO9781139541022.004.
- 545 2. Angelaki, D. E. *et al.* A gravity-based three-dimensional compass in the mouse brain. *Nat. Commun.*  
546 **11**, 1855 (2020).
- 547 3. Mimica, B., Dunn, B. A., Tombaz, T., Bojja, V. P. T. N. C. S. & Whitlock, J. R. Efficient cortical  
548 coding of 3D posture in freely behaving rats. *Science* **362**, 584–589 (2018).
- 549 4. Shemesh, Y. *et al.* High-order social interactions in groups of mice. *eLife* **2**, e00759 (2013).
- 550 5. Weissbrod, A. *et al.* Automated long-term tracking and social behavioural phenotyping of animal  
551 colonies within a semi-natural environment. *Nat. Commun.* **4**, 1–10 (2013).
- 552 6. Mathis, A. *et al.* DeepLabCut: markerless pose estimation of user-defined body parts with deep  
553 learning. *Nat. Neurosci.* **21**, 1281–1289 (2018).
- 554 7. Pereira, T. D. *et al.* Fast animal pose estimation using deep neural networks. *Nat. Methods* **16**, 117–  
555 125 (2019).
- 556 8. Graving, J. M. *et al.* DeepPoseKit, a software toolkit for fast and robust animal pose estimation us-  
557 ing deep learning. *eLife* **8**, e47994 (2019).
- 558 9. Nath, T. *et al.* Using DeepLabCut for 3D markerless pose estimation across species and behaviors.  
559 *Nat. Protoc.* **14**, 2152–2176 (2019).
- 560 10. Bala, P. C. *et al.* OpenMonkeyStudio: Automated Markerless Pose Estimation in Freely Moving Ma-  
561 caques. *bioRxiv* 2020.01.31.928861 (2020) doi:10.1101/2020.01.31.928861.
- 562 11. Matsumoto, J. *et al.* A 3D-Video-Based Computerized Analysis of Social and Sexual Interactions in  
563 Rats. *PLOS ONE* **8**, e78460 (2013).
- 564 12. Nakamura, T. *et al.* A Markerless 3D Computerized Motion Capture System Incorporating a Skele-  
565 ton Model for Monkeys. *PLOS ONE* **11**, e0166154 (2016).
- 566 13. Wiltschko, A. B. *et al.* Mapping Sub-Second Structure in Mouse Behavior. *Neuron* **88**, 1121–1135  
567 (2015).
- 568 14. Newell, A., Yang, K. & Deng, J. Stacked Hourglass Networks for Human Pose Estimation.  
569 *ArXiv160306937 Cs* (2016).
- 570 15. Günel, S. *et al.* DeepFly3D, a deep learning-based approach for 3D limb and appendage tracking in  
571 tethered, adult *Drosophila*. *eLife* **8**, e48571 (2019).
- 572 16. Cao, Z., Simon, T., Wei, S.-E. & Sheikh, Y. Realtime Multi-Person 2D Pose Estimation using Part  
573 Affinity Fields. *ArXiv161108050 Cs* (2017).
- 574 17. Shorten, C. & Khoshgoftaar, T. M. A survey on Image Data Augmentation for Deep Learning. *J. Big*  
575 *Data* **6**, 60 (2019).
- 576 18. Transtrum, M. K., Machta, B. B. & Sethna, J. P. Geometry of nonlinear least squares with applica-  
577 tions to sloppy models and optimization. *Phys. Rev. E* **83**, 036701 (2011).
- 578 19. Hart, J. C. Distance to an ellipsoid. in *Graphics Gems* (ed. Heckbert, P.) vol. 1994 113–119 (Aca-  
579 demic Press).
- 580 20. Kleinsteuber, M. & Hüper, K. Approximate Geometric Ellipsoid Fitting: A CG-Approach. in *Recent*  
581 *Advances in Optimization and its Applications in Engineering* (eds. Diehl, M., Glineur, F., Jarle-  
582 bring, E. & Michiels, W.) 73–82 (Springer, 2010). doi:10.1007/978-3-642-12598-0\_7.
- 583 21. Wang, W., Wang, J. & Kim, M.-S. An algebraic condition for the separation of two ellipsoids. *Com-*  
584 *put. Aided Geom. Des.* **18**, 531–539 (2001).
- 585 22. Choset, H. M. *Principles of robot motion: theory, algorithms, and implementation*. (MIT Press,  
586 2005).
- 587 23. Deutscher, J. & Reid, I. Articulated Body Motion Capture by Stochastic Search. *Int. J. Comput. Vis.*  
588 **61**, 185–205 (2005).

- 589 24. Lázaro-Gredilla, M., Van Vaerenbergh, S. & Santamaría, I. A Bayesian approach to tracking with  
590 kernel recursive least-squares. in *2011 IEEE International Workshop on Machine Learning for Sig-*  
591 *nal Processing* 1–6 (2011). doi:10.1109/MLSP.2011.6064585.
- 592 25. Paszke, A. *et al.* PyTorch: An Imperative Style, High-Performance Deep Learning Library. in *Ad-*  
593 *vances in Neural Information Processing Systems 32* (eds. Wallach, H. *et al.*) 8024–8035 (Curran  
594 Associates, Inc., 2019).
- 595 26. Chaumont, F. de *et al.* Real-time analysis of the behaviour of groups of mice via a depth-sensing  
596 camera and machine learning. *Nat. Biomed. Eng.* **3**, 930–942 (2019).
- 597 27. Sobol, I. M. On the distribution of points in a cube and the approximate evaluation of integrals.  
598 *USSR Comput. Math. Math. Phys.* **7**, 86–112 (1967).
- 599 28. Das, G. Top-k Algorithms and Applications. in *Database Systems for Advanced Applications* (eds.  
600 Zhou, X., Yokota, H., Deng, K. & Liu, Q.) 789–792 (Springer, 2009). doi:10.1007/978-3-642-  
601 00887-0\_74.
- 602 29. Murray, L. M., Lee, A. & Jacob, P. E. Parallel Resampling in the Particle Filter. *J. Comput. Graph.*  
603 *Stat.* **25**, 789–805 (2016).
- 604 30. Rauch, H. E., Tung, F. & Striebel, C. T. Maximum likelihood estimates of linear dynamic systems.  
605 *AIAA J.* **3**, 1445–1450 (1965).
- 606 31. Simon, D. *Optimal State Estimation: Kalman, H $\infty$ , and Nonlinear Approaches*. (John Wiley & Sons,  
607 Inc., 2006). doi:10.1002/0470045345.
- 608 32. Landis, M. F., Cheng, Y., Crassidis, J. L. & Oshman, Y. Averaging quaternions. *J. Guid. Control*  
609 *Dyn.* **30**, 1193–1197 (2007).
- 610 33. Barnett, S. A. *The rat: A study in behaviour*. xvi, 248 (Aldine, 1963).
- 611 34. Wolfe, J., Mende, C. & Brecht, M. Social facial touch in rats. *Behav. Neurosci.* **125**, 900–910 (2011).
- 612 35. Bingham, E. *et al.* Pyro: Deep Universal Probabilistic Programming. *ArXiv181009538 Cs Stat*  
613 (2018).
- 614 36. Fox, E., Sudderth, E., Jordan, M. & Willsky, A. Bayesian Nonparametric Methods for Learning Mar-  
615 kov Switching Processes. *IEEE Signal Process. Mag.* 5563110 (2010)  
616 doi:10.1109/MSP.2010.937999.
- 617 37. Tombaz, T. *et al.* Action representation in the mouse parieto-frontal network. *Sci. Rep.* **10**, 1–14  
618 (2020).
- 619 38. Díaz López, B. When personality matters: personality and social structure in wild bottlenose dol-  
620 phins, *Tursiops truncatus*. *Anim. Behav.* **163**, 73–84 (2020).
- 621 39. Tao, L., Ozarkar, S., Beck, J. M. & Bhandawat, V. Statistical structure of locomotion and its modula-  
622 tion by odors. *eLife* **8**, e41235 (2019).
- 623 40. Porcelli, S. *et al.* Social brain, social dysfunction and social withdrawal. *Neurosci. Biobehav. Rev.*  
624 **97**, 10–33 (2019).
- 625 41. Uchino, B. N. *et al.* Social support, social integration, and inflammatory cytokines: A meta-analysis.  
626 *Health Psychol. Off. J. Div. Health Psychol. Am. Psychol. Assoc.* **37**, 462–471 (2018).
- 627 42. Che, X., Cash, R., Ng, S. K., Fitzgerald, P. & Fitzgibbon, B. M. A Systematic Review of the Pro-  
628 cesses Underlying the Main and the Buffering Effect of Social Support on the Experience of Pain.  
629 *Clin. J. Pain* **34**, 1061–1076 (2018).
- 630 43. Buzsáki, G. *et al.* Tools for Probing Local Circuits: High-Density Silicon Probes Combined with  
631 Optogenetics. *Neuron* **86**, 92–105 (2015).
- 632 44. Steinmetz, N. A., Koch, C., Harris, K. D. & Carandini, M. Challenges and opportunities for large-  
633 scale electrophysiology with Neuropixels probes. *Curr. Opin. Neurobiol.* **50**, 92–100 (2018).
- 634 45. Aharoni, D. & Hoogland, T. M. Circuit Investigations With Open-Source Miniaturized Microscopes:  
635 Past, Present and Future. *Front. Cell. Neurosci.* **13**, (2019).
- 636 46. Klioutchnikov, A. *et al.* Three-photon head-mounted microscope for imaging deep cortical layers in

- 637 freely moving rats. *Nat. Methods* **17**, 509–513 (2020).
- 638 47. Krakauer, J. W., Ghazanfar, A. A., Gomez-Marin, A., MacIver, M. A. & Poeppel, D. Neuroscience  
639 Needs Behavior: Correcting a Reductionist Bias. *Neuron* **93**, 480–490 (2017).
- 640 48. Datta, S. R., Anderson, D. J., Branson, K., Perona, P. & Leifer, A. Computational Neuroethology: A  
641 Call to Action. *Neuron* **104**, 11–24 (2019).
- 642 49. Berman, G. J., Choi, D. M., Bialek, W. & Shaevitz, J. W. Mapping the stereotyped behaviour of  
643 freely moving fruit flies. *J. R. Soc. Interface* **11**, 20140672 (2014).
- 644 50. Berman, G. J., Bialek, W. & Shaevitz, J. W. Predictability and hierarchy in *Drosophila* behavior.  
645 *Proc. Natl. Acad. Sci.* **113**, 11943–11948 (2016).
- 646 51. Werkhoven, Z. *et al.* The structure of behavioral variation within a genotype. *bioRxiv* 779363 (2019)  
647 doi:10.1101/779363.
- 648 52. Klibaite, U., Berman, G. J., Cande, J., Stern, D. L. & Shaevitz, J. W. An unsupervised method for  
649 quantifying the behavior of paired animals. *Phys. Biol.* **14**, 015006 (2017).
- 650 53. Klibaite, U. & Shaevitz, J. W. Interacting fruit flies synchronize behavior. *bioRxiv* 545483 (2019)  
651 doi:10.1101/545483.
- 652 54. Braun, E., Geurten, B. & Egelhaaf, M. Identifying Prototypical Components in Behaviour Using  
653 Clustering Algorithms. *PLOS ONE* **5**, e9361 (2010).
- 654 55. Mearns, D. S., Donovan, J. C., Fernandes, A. M., Semmelhack, J. L. & Baier, H. Deconstructing  
655 Hunting Behavior Reveals a Tightly Coupled Stimulus-Response Loop. *Curr. Biol.* **30**, 54–69.e9  
656 (2020).
- 657 56. Markowitz, J. E. *et al.* The Striatum Organizes 3D Behavior via Moment-to-Moment Action Selec-  
658 tion. *Cell* **174**, 44–58.e17 (2018).
- 659 57. Johnson, R. E. *et al.* Probabilistic Models of Larval Zebrafish Behavior Reveal Structure on Many  
660 Scales. *Curr. Biol.* **30**, 70–82.e4 (2020).
- 661 58. DeRuiter, S. L. *et al.* A multivariate mixed hidden Markov model to analyze blue whale diving be-  
662 haviour during controlled sound exposures. *ArXiv160206570 Q-Bio Stat* (2016).
- 663 59. Adam, T. *et al.* Joint modelling of multi-scale animal movement data using hierarchical hidden Mar-  
664 kov models. *Methods Ecol. Evol.* **10**, 1536–1550 (2019).
- 665 60. Hsu, A. I. & Yttri, E. A. *B-SOiD: An Open Source Unsupervised Algorithm for Discovery of Sponta-  
666 neous Behaviors.* <http://biorxiv.org/lookup/doi/10.1101/770271> (2019) doi:10.1101/770271.
- 667 61. Linderman, S. W. *et al.* Recurrent switching linear dynamical systems. *ArXiv161008466 Stat* (2016).
- 668 62. Blei, D. M., Kucukelbir, A. & McAuliffe, J. D. Variational Inference: A Review for Statisticians. *J.*  
669 *Am. Stat. Assoc.* **112**, 859–877 (2017).
- 670 63. Pohle, J., Langrock, R., van Beest, F. M. & Schmidt, N. M. Selecting the Number of States in Hid-  
671 den Markov Models: Pragmatic Solutions Illustrated Using Animal Movement. *J. Agric. Biol. Envi-  
672 ron. Stat.* **22**, 270–293 (2017).
- 673 64. Javer, A., Ripoll-Sánchez, L. & Brown, A. E. X. Powerful and interpretable behavioural features for  
674 quantitative phenotyping of *Caenorhabditis elegans*. *Philos. Trans. R. Soc. B Biol. Sci.* **373**,  
675 20170375 (2018).
- 676 65. Kropff, E., Carmichael, J. E., Moser, M.-B. & Moser, E. I. Speed cells in the medial entorhinal cor-  
677 tex. *Nature* **523**, 419–424 (2015).
- 678 66. Georgopoulos, A. P., Kalaska, J. F., Caminiti, R. & Massey, J. T. On the relations between the direc-  
679 tion of two-dimensional arm movements and cell discharge in primate motor cortex. *J. Neurosci.* **2**,  
680 1527–1537 (1982).
- 681 67. Kalaska, J. F. The representation of arm movements in postcentral and parietal cortex. *Can. J. Phys-  
682 iol. Pharmacol.* **66**, 455–463 (1988).
- 683 68. Guo, Y. *et al.* Deep Learning for 3D Point Clouds: A Survey. *ArXiv191212033 Cs Eess* (2019).

- 684 69. Novotny, D., Ravi, N., Graham, B., Neverova, N. & Vedaldi, A. C3DPO: Canonical 3D Pose Net-  
685 works for Non-Rigid Structure From Motion. *ArXiv190902533 Cs* (2019).
- 686 70. Sanakoyeu, A., Khalidov, V., McCarthy, M. S., Vedaldi, A. & Neverova, N. Transferring Dense Pose  
687 to Proximal Animal Classes. *ArXiv200300080 Cs* (2020).
- 688 71. Zuffi, S., Kanazawa, A., Berger-Wolf, T. & Black, M. J. Three-D Safari: Learning to Estimate Zebra  
689 Pose, Shape, and Texture from Images ‘In the Wild’. *ArXiv190807201 Cs* (2019).
- 690 72. Gkioxari, G., Malik, J. & Johnson, J. Mesh R-CNN. *ArXiv190602739 Cs* (2020).
- 691 73. Niemeyer, M., Mescheder, L., Oechsle, M. & Geiger, A. Occupancy Flow: 4D Reconstruction by  
692 Learning Particle Dynamics. in *2019 IEEE/CVF International Conference on Computer Vision*  
693 *(ICCV)* 5378–5388 (IEEE, 2019). doi:10.1109/ICCV.2019.00548.
- 694 74. Fey, M. & Lenssen, J. E. Fast Graph Representation Learning with PyTorch Geometric.  
695 *ArXiv190302428 Cs Stat* (2019).
- 696 75. Jatavallabhula, K. M. *et al.* Kaolin: A PyTorch Library for Accelerating 3D Deep Learning Research.  
697 *ArXiv191105063 Cs* (2019).
- 698 76. Ravi, N. *et al.* *PyTorch3D*. (2020).
- 699 77. Deng, B. *et al.* NASA: Neural Articulated Shape Approximation. *ArXiv191203207 Cs* (2020).
- 700 78. Zuffi, S., Kanazawa, A., Jacobs, D. & Black, M. J. 3D Menagerie: Modeling the 3D shape and pose  
701 of animals. *ArXiv161107700 Cs* (2017).
- 702 79. Min, S., Won, J., Lee, S., Park, J. & Lee, J. SoftCon: Simulation and Control of Soft-Bodied Ani-  
703 mals with Biomimetic Actuators. *ACM Trans. Graph.* **38**, (2019).
- 704 80. Pereira, T. D., Tabris, N., Turner, D., Shaevitz, J. & Murthy, M. <https://sleap.ai/>. <https://sleap.ai/>  
705 (2020).
- 706 81. Gillis, W. *et al.* Revealing elements of naturalistic reinforcement learning through closed-loop action  
707 identification. in *2019 Neuroscience Meeting Planner* Program No. 146.17 (Society for Neurosci-  
708 ence, 2019).
- 709 82. Gardner, J. R., Pleiss, G., Bindel, D., Weinberger, K. Q. & Wilson, A. G. GPyTorch: Blackbox Ma-  
710 trix-Matrix Gaussian Process Inference with GPU Acceleration. *ArXiv180911165 Cs Stat* (2019).

711 **ACKNOWLEDGEMENTS**

712 This work was supported by The Novo Nordisk Foundation (C.L.E.), the BRAIN Initiative (NS107616 to  
713 R.C.F.) and a Howard Hughes Medical Institute Faculty Scholarship (R.C.F.).

714

715 **AUTHOR CONTRIBUTIONS**

716 C.L.E. designed and implemented the system, performed experiments, and analyzed the data. R.C.F. super-  
717 vised the study. C.L.E and R.C.F. wrote the manuscript.

718

719 **COMPETING INTERESTS**

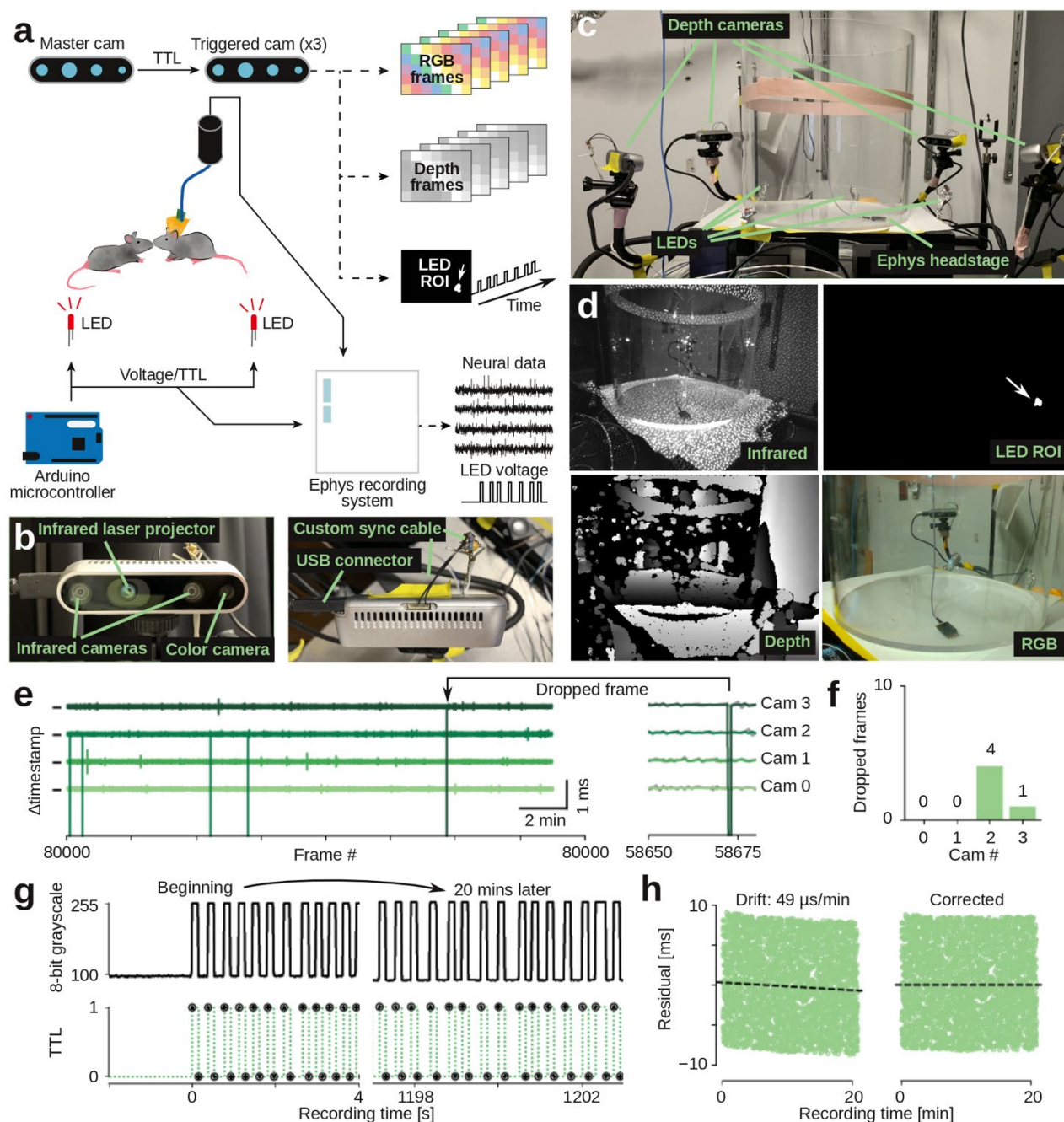
720 The authors declare no competing interests.

721

722 **DATA AND CODE AVAILABILITY**

723 All code and an example dataset were submitted with this manuscript. All code and an example dataset will  
724 be available on Github before or upon publication.

725 FIGURES



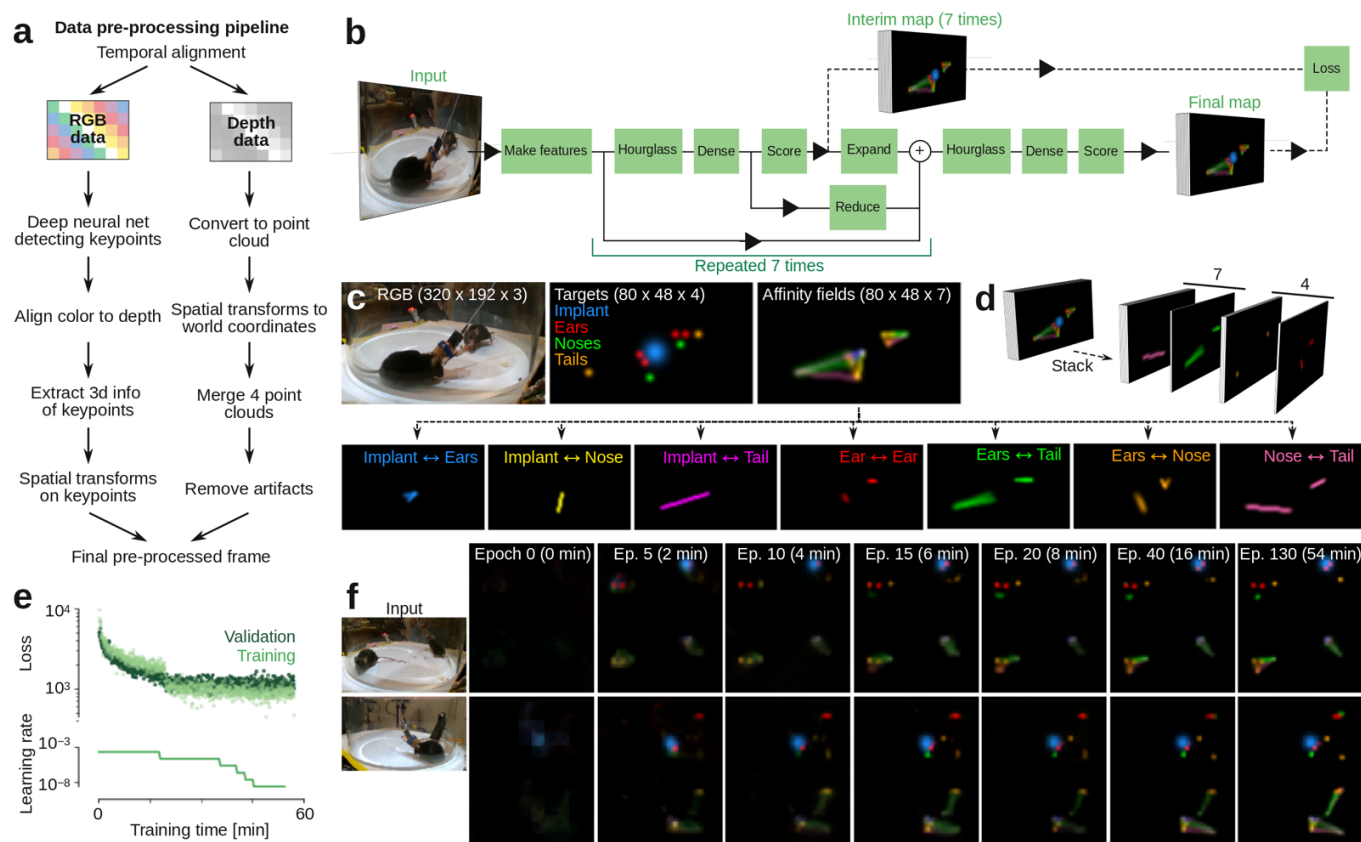
726

727 **Figure 1. Raw data acquisition, temporal alignment and recording stability.** **a**, Schematic of recording  
 728 setup, showing flow of synchronization pulses and raw data. We use a custom Python program to record RGB  
 729 images, depth images, and state (on/off) of synchronization LEDs from all four cameras. Neural data and TTL  
 730 state of LEDs are recorded with a standard electrophysiology recording system. We use a custom Python  
 731 program to record video frames over USB (60 frames/s) and automatically deliver LED synchronization

732 pulses with randomized delays via Arduino microcontroller. **b**, Close-up images of the depth cameras, show-  
733 ing the two infrared sensors, color sensor, and cables for data transfer and synchronization. **c**, Photograph of  
734 recording setup, showing the four depth cameras, synchronization LEDs, and circular behavioral arena (trans-  
735 parent acrylic, 12" diameter). **d**, Example raw data images (top left: single infrared image with visible infrared  
736 laser dots; top right: corresponding automatically-generated mask image for recording LED synchronization  
737 state (arrow, LED location); bottom left: corresponding depth image, estimated from binocular disparity be-  
738 tween two infrared images; bottom right: corresponding color image). **e**, Inter-frame-interval from four cam-  
739 eras (21 min of recording). Vertical ticks indicate 16.66 ms (corresponding to 60 frames/s), individual cameras  
740 are colored and vertically offset. Frame rate is very stable (jitter across all cameras:  $\pm 26 \mu\text{s}$ ). Arrow, example  
741 dropped frame. **f**, Number of dropped frames across the example 21 min recording. **g**, Top row, LED state  
742 (on/off) as captured by one camera (the 8-bit value of central pixel of LED ROI mask), at start of recording  
743 and after 20 minutes of recording. Bottom row, aligned LED trace, as recorded by electrophysiology recording  
744 system. **h**, Temporal residuals between recorded camera LED trace (**g**, top) and recorded TTL LED trace (**g**,  
745 bottom) are stable, but drift slightly ( $49 \mu\text{s}/\text{min}$ , left panel). We can automatically detect and correct for this  
746 small drift (right panel).

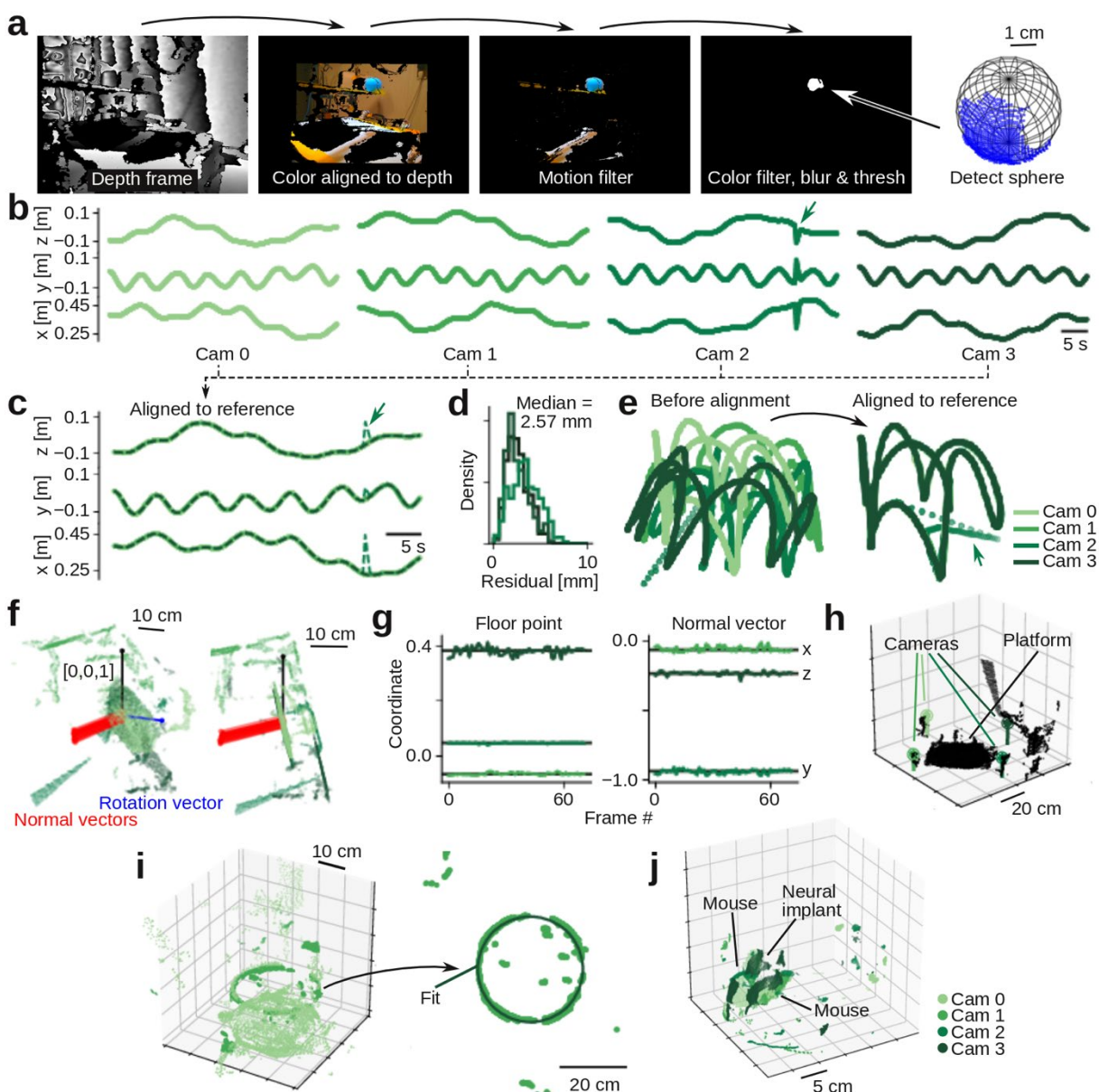
747





748

749 **Figure 2. Detection of body key-points with a deep convolutional neural network.** **a**, Workflow for pre-  
 750 processing of raw image data. **b**, Example training data for the deep convolutional neural network. The net-  
 751 work is trained to output four types of body key-points (Implant, Ears, Noses, Tails) and seven 1-D affinity  
 752 fields, connecting key-points within each body. **c**, Example of full training target tensor. **d**, The ‘stacked hour-  
 753 glass’ convolutional network architecture. Each ‘hourglass’ block of the network uses pooling and upsampling  
 754 to incorporate both fine (high-resolution) and large-scale (low-resolution) information in the target prediction.  
 755 The hourglass and scoring blocks are repeated seven times (seven ‘stacks’), such that intermediate key-point  
 756 and affinity field predictions feed into subsequent hourglass blocks. Both the intermediate and final target  
 757 maps contribute to the training loss, but only the final output map is used for prediction. **e**, Convergence plot  
 758 of example training set. Top, loss function for each mini-batch of the training set (526 images) and validation  
 759 set (50 images). Bottom, learning rate. Network loss is trained (plateaued) after ~ 60 minutes. **f**, Network  
 760 performance as function of training epoch for two example images in the validation set. Left, input images;  
 761 right, final output maps for key-points and affinity fields.



762

763 **Figure 3. Depth data alignment and pre-processing.** **a**, Calibration ball detection pipeline. We use a com-

764 bination of motion filtering, color filtering, and smoothing filters to detect and extract 3D ball surface. We

765 estimate 3D location of the ball by fitting a sphere to the extracted surface. **b**, Estimated 3D trajectories of

766 calibration ball as seen by the four cameras. One trajectory has an error (arrow) where ball trajectory was out

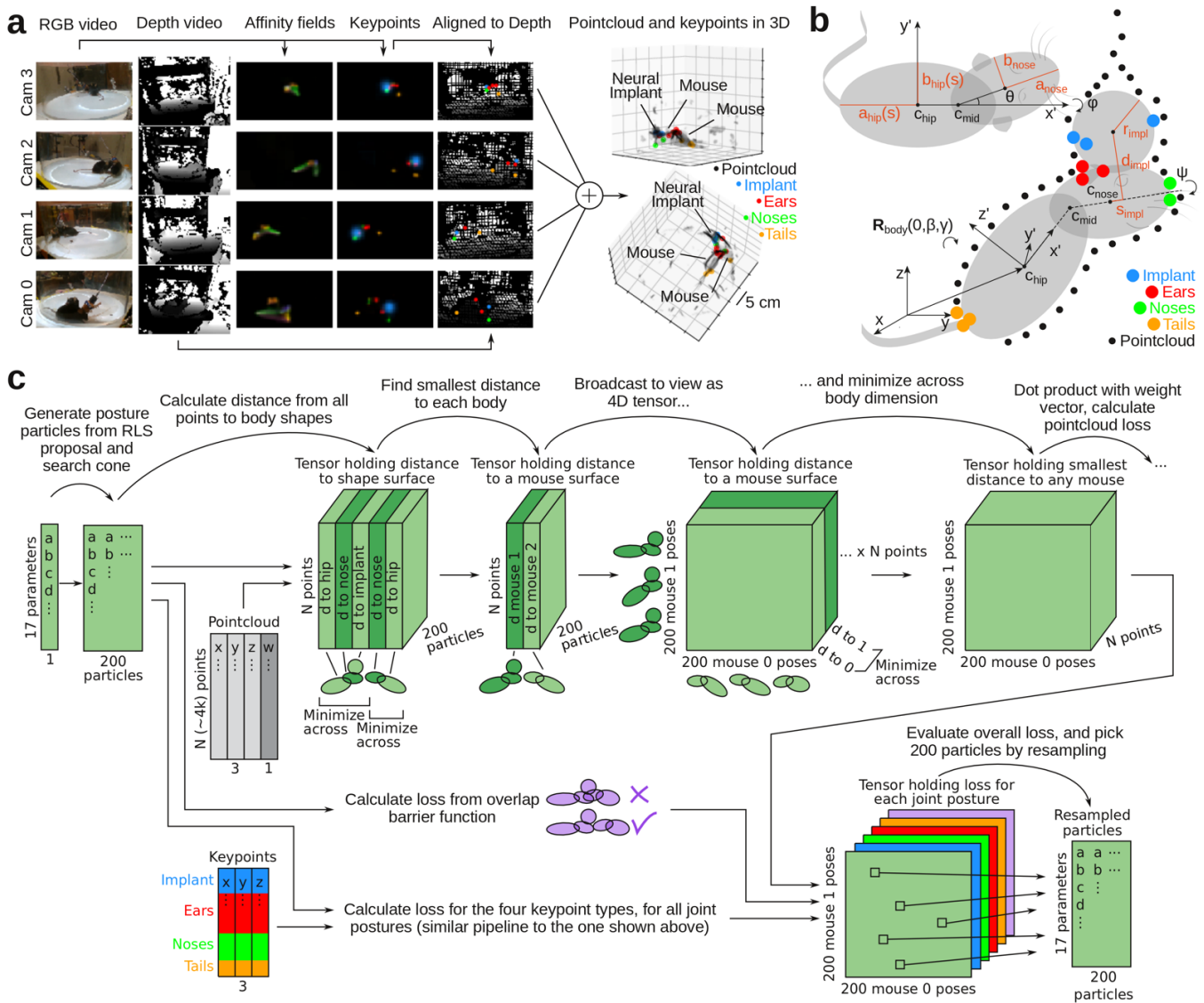
767 of view. **c**, Overlay of trajectories after alignment in time and space. Our alignment pipeline uses a robust

768 regression method and is insensitive to errors (arrow) in the calibration ball trajectory. **d**, Distribution of

769 residuals, using cam 0 as reference. **e**, Estimated trajectory in 3D space, before and after alignment of camera

770 data. **f**, Example frame used in automatic detection of the behavioral arena location. Show are pixels from the

771 four cameras, after alignment (green), estimated normal vectors to the behavioral platform floor (red), the  
772 estimated rotation vector (blue), and the reference vector (unit vector along z-axis, black). **g**, Estimated loca-  
773 tion (left) and normal vector (right) to the behavioral platform floor, across 60 random frames. **h**, Example  
774 frame, after rotating the platform into the xy-plane, and removing pixels below and outside the arena. Inferred  
775 camera locations are indicated with stick and ball. **i**, Automatic detection of behavioral arena location. **j**, Ex-  
776 ample 3D frame, showing merged data from four cameras, after automatic removal of the arena floor and  
777 imaging artifacts induced by the acrylic cylinder. Colors, which camera captured the pixels.



778

779 **Figure 4. Mouse body model and fully vectorized, GPU-executable tracking algorithm. a**, Full assembly

780 pipeline for a single pre-processed data frame, going from raw RGB and depth images (left columns) to as-

781 sembled 3D point-cloud (black dots, right) and body key-point positions in 3D space (colored dots, right). **b**,

782 Schematic depiction of mouse body model (grey, deformable ellipsoids) and implant model (grey sphere), fit

783 to point-cloud (black dots) and body key-points (colored dots). The loss function assigns loss to distance from

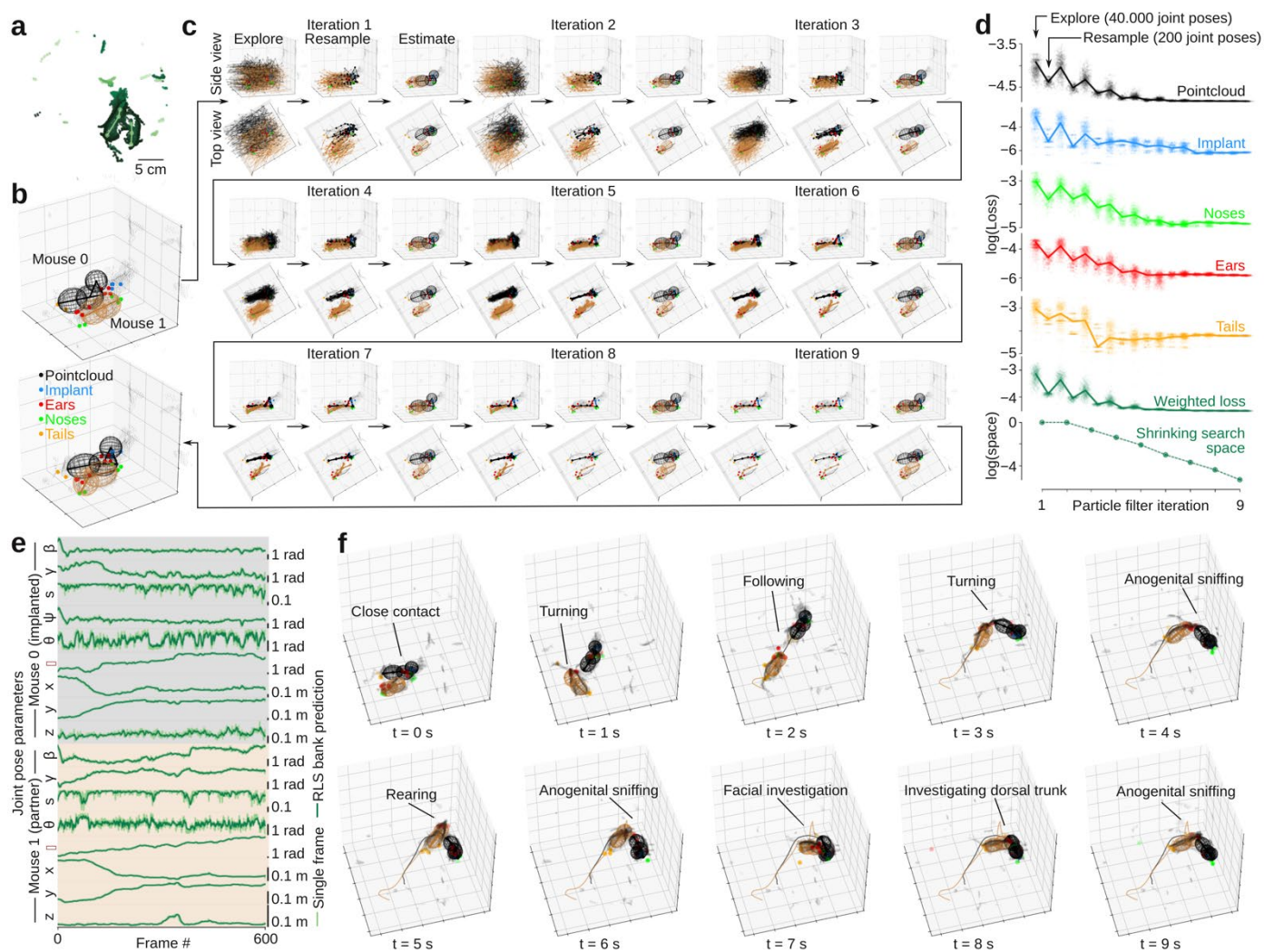
784 the point-cloud to the body model surface (black arrows) and from key-point locations to landmark locations

785 on the body model (e.g., from nose key-points to the tip of the nose ellipsoids; colored arrows). **c**, Schematic

786 of loss function calculation and tracking algorithm. All operations implemented as GPU-accelerated tensor

787 algebra.

788



789

790 **Figure 5. Particle filter convergence and examples of tracked behavioral data.** **a**, Tracking algorithm is

791 initialized by manual clicking of approximate locations of the two animals (light green dots, lines) on a top-

792 down view of the behavioral arena (dark green dots, shade indicates z-coordinate). **b**, 3D view of initialized

793 body model (top) and fitted body model (bottom) after running tracking algorithm on the frame. Black

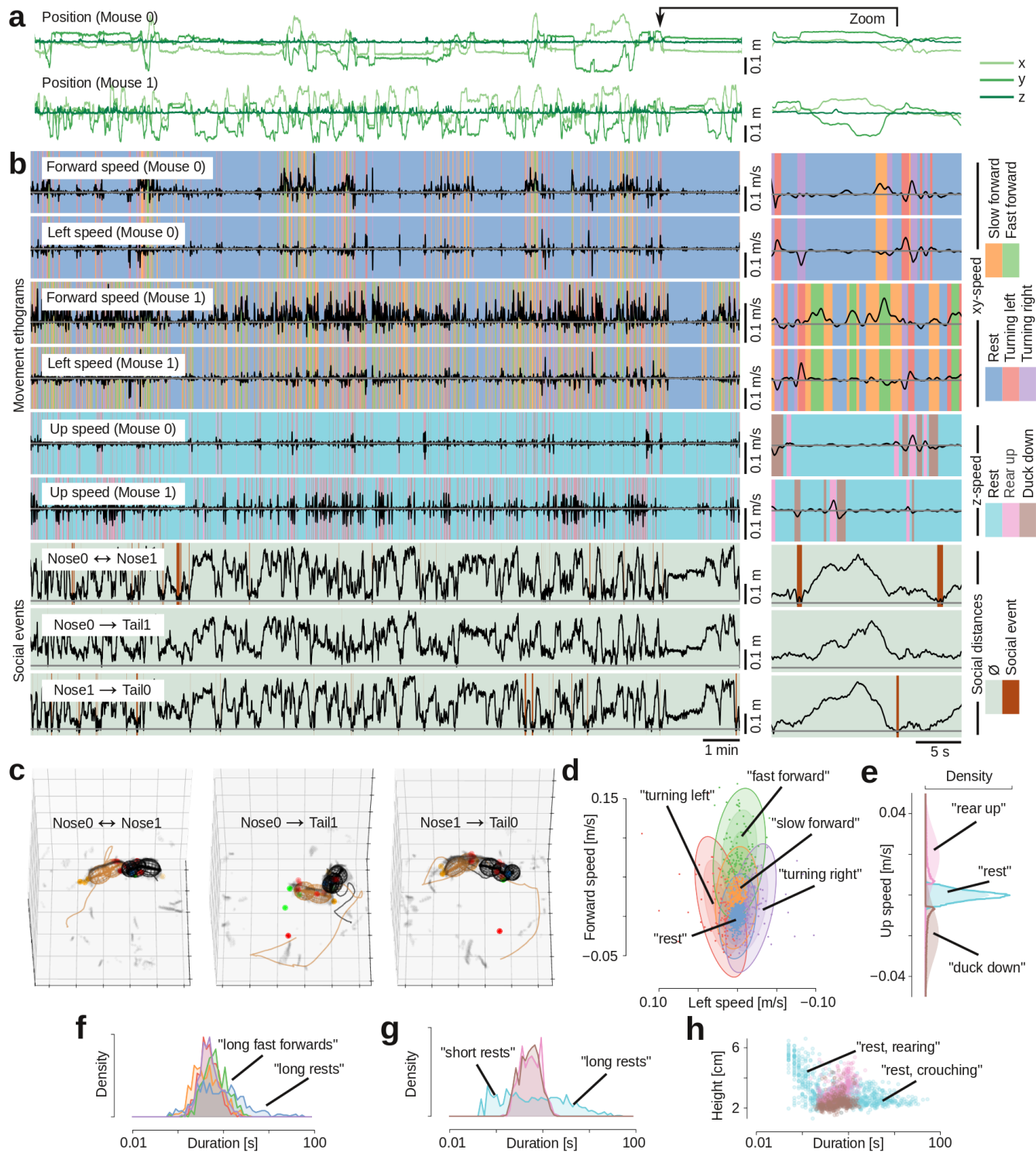
794 wireframe model, implanted mouse; brown wireframe model, partner animal. **c**, Particle filter state across 9

795 iterations of the fitting algorithm. After iteration 2, we shrink ('anneal') the exploration space with each step.

796 **d**, Loss function values and size of filter search space across filter iterations. **e**, Tracked data (light green) and

797 running adaptive estimate (dark green) across 600 frames (10 s). **f**, Data and fitted joint posture model, across

798 10 seconds of behavior. Trailing lines, location of hip ellipsoid center in last 10 seconds.



799

800 **Figure 6. Automatic classification of movement patterns and behavioral states during social interactions.**

801 **tions. a**, Tracked position of both mice, across an example 21 min recording. **b**, Extracted behavioral fea-

802 **tures: three speed components (forward, left and up in the mice's egocentric reference frames), and three**

803 ‘social distances’ (nose-to-nose distance and two nose-to-tail distances). Colors indicate ethograms of auto-  
804 matically detected behavioral states. **c**, Examples of identified social events: nose-to-nose-touch, and ano-  
805 genital nose-contacts. **e**, Mean and covariance (3 standard deviations indicated by ellipsoids) for each latent  
806 state for the forward/leftward running (dots indicate a subsample of tracked speeds, colored by their most  
807 likely latent state) **e**, Mean and variance of latent states in the  $z$ -plane (shaded color) as well as distribution  
808 of tracked data assigned to those latent states (histograms) **f**, Distribution of the duration of the five behav-  
809 ioral states in the  $xy$ -plane. Periods of rest (blue) are the longest ( $p < 0.05$ , Mann-Whitney U-test) and bouts  
810 of fast forward movement (green) are to be longer other movement bouts ( $p < 0.001$ , Mann-Whitney U-  
811 test). **g**, Distribution of duration of the three behavioral states in the  $z$ -plane. Periods of rest (light blue) are  
812 either very short or very long. **h**, Plot of body elevation against behavior duration. Short periods of rest hap-  
813 pen when the  $z$ -coordinate is high (the mouse rears up, waits for a brief moment before ducking back down),  
814 whereas long periods of rest happen when the  $z$ -coordinate is low (when the mouse is resting or moving  
815 around the arena,  $\rho = -0.47$ ,  $p < 0.001$ , Spearman rank).

816 **METHODS**

817

818 **Hardware**

819

820 Necessary hardware:

821

Item	Recommendation	Price (USD)	N	Total (USD)
Depth cameras	<a href="#">Intel RealSense D435</a>	179.00	4	716.00
Camera stands	<a href="#">Etubby 26" gooseneck webcam stand</a>	24.96	4	99.84
PCIe card with 4 independent USB 3.0 controllers	<a href="#">Startech 4-port superspeed</a>	83.54	1	83.54
Active, repeating USB 3.0 cables	<a href="#">UGREEN, USB 3.0 Active Repeater Cable</a>	18.89	4	75.56
Arduino with USB cable	<a href="#">Arduino Uno R3</a>	13.98	1	13.98
Pytorch-compatible GPU	<a href="#">Any NVIDIA card with CUDA support</a>	500.00	1	500.00
Behavioral arena (acrylic cylinder or elevated platform)	<a href="#">12"-diameter, 5/32" thick acrylic cylinder</a>	71.20	1	71.20
Depth camera GPIO pin connector (jumper)	<a href="#">JST ASSHSSH28K305</a>	0.54	8	4.32
Depth camera GPIO pin connector (jumper housing)	<a href="#">JST SHR-09V-S</a>	0.19	4	0.76
Colored ping-pong balls (for calibration)	<a href="#">Stiga 40 mm ITTF Regulation size</a>	6.64	1	6.64
Total				1571.84

822

823 General lab electronics (tape, wire, soldering equipment, etc.) and:

824

Item	N
Infrared or red LEDs	4
0.1" pin headers or jumper wires	2
20 kOhm resistors	4
22 nF capacitors	4
200 Ohm resistor (or same order of magnitude)	1
Stick (for moving ping-pong ball during calibration)	1

825

826



827 ***Software***

828 Our system uses the following software: Linux (tested on Ubuntu 16.04 LTE, but should work on others,  
829 <https://ubuntu.com/>), Intel Realsense SDK (<https://github.com/IntelRealSense/librealsense>), Python (tested  
830 on Python 3.6, we recommend Anaconda, <https://www.anaconda.com/distribution/>). Required Python pack-  
831 ages will be installed with PIP or conda (script in supplementary software). All required software is free and  
832 open source.

833

834 ***Animal welfare***

835 All experimental procedures were performed according to animal welfare laws under the supervision of lo-  
836 cal ethics committees. Animals were kept on a 12hr/12hr light cycle with ad libitum access to food and wa-  
837 ter. Mice presented as partner animals were housed socially in same-sex cages, and post-surgery implanted  
838 animals were housed in single animal cages. Neural recordings electrodes were implanted on the dorsal  
839 skull under isoflurane anesthesia, with a 3D-printed electrode drive and a hand-built mesh housing. All pro-  
840 cedures were approved under NYU School of Medicine IACUC protocols.

841

842 ***Recording data structure***

843 The Python program is set to pull raw images at 640 x 480 (color) and 640 x 480 (depth), but only saves 320  
844 x 210 (color) and 320 x 240 (depth). We do this to reduce noise (multi-pixel averaging), save disk space and  
845 reduce processing time. Our software also works for saving images up to 848 x 480 (color) and 848 x 480  
846 (depth) at 60 frames/s, in case the system is to be used for a bigger arena, or to detect smaller body parts (eyes,  
847 paws, etc). Images were transferred from the cameras with the python bindings for the Intel Realsense SDK  
848 (<https://github.com/IntelRealSense/librealsense>), and saved as 8-bit, 3-channel PNG files with opencv (for  
849 color images) or as 16-bit binary files (for depth images).

850

### 851 ***3D data structure***

852 For efficient access and storage of the large datasets, we save all pre-processed data to hdf5 files. Because the  
853 number of data points (point-cloud and key-points) per frame varies, we save every frame as a jagged array.  
854 To this end, we pack all pre-processed data to a single array. If we detect N points in the point-cloud and M  
855 key-points in the color images, we save a stack of the 3D coordinates of the points in the point-cloud (Nx3,  
856 raveled to 3N), the weights (N), the 3D coordinates of the key-points (Mx3, raveled to 3M), their pseudo-  
857 posterior (M), an index indicating key-point type (M), and the number of key-points (1). Functions to pack  
858 and unpack the pre-processed data from a single line ('pack\_to\_jagged' and 'unpack\_from\_jagged') are pro-  
859 vided.

860

### 861 ***Temporal synchronization***

862 LED blinks were generated with voltage pulses from an Arduino (on digital pin 12), controlled over USB  
863 with a python interface for the Firmata protocol (<https://github.com/tino/pyFirmata>). To receive the Firmata  
864 messages, the Arduino was flashed with the 'StandardFirmata' example, that comes with the standard Arduino  
865 IDE. TTL pulses were 150 ms long and spaced by  $\sim U(150,350)$  ms.. We recorded the emitted voltage pulses  
866 in both the infrared images (used to calculate the depth image) and on a TTL input on an Open Ephys Acqui-  
867 sition System (<https://open-ephys.org/>). We detected LED blinks and TTL flips by threshold crossing and  
868 roughly aligned the two signals by the first detected blink/flip. We first refined the alignment by cross corre-  
869 lation in 10 ms steps, and then identified pairs of blinks/flips by detecting the closest blink, subject to a cutoff  
870 ( $zscore < 2$ , compared to all blink-to-flip time differences) to remove blinks missed by the camera (because  
871 an experimenter moved an arm in front of a camera to place a mouse in the arena, for example). The final  
872 shift and drift was estimated by a robust regression (Theil-Sen estimator) on the pairs of blinks/links.

873

### 874 ***Deep neural network***

875 We used a stacked hourglass network<sup>14</sup> implemented in Pytorch<sup>25</sup> (<https://github.com/pytorch/pytorch>). The  
876 network architecture code is from the implementation in ‘PyTorch-Pose’  
877 (<https://github.com/bearpaw/pytorch-pose>). The full network architecture is shown in **Supplementary Fig 1**.  
878 The Image augmentation during training was done with the ‘imgaug’ library ([https://github.com/aleju/im-](https://github.com/aleju/imgaug)  
879 [gaug](https://github.com/aleju/imgaug)). Our augmentation pipeline is shown in Supplementary Fig. 3. The network was trained by RMSProp  
880 ( $\alpha = 0.99$ ,  $\epsilon = 10^{-8}$ ) with an initial learning rate of 0.00025. During training, the learning rate was automatically  
881 reduced by a factor of 10 if the training loss decreased by less than 0.1% for five successive steps (using the  
882 built-in learning rate scheduler in Pytorch). After training, we used the final output map of the network for  
883 key-point detection, and used a maximum filter to detect key-point locations as local maxima in network  
884 output images with a posterior pseudo-probability of at least 0.5.

885

### 886 *Image labeling and target maps*

887 For training the network to recognize body parts, we need to generate labeled frames by manual annotation.  
888 For each frame, 1-5 body parts are labeled on the implanted animal and 1-4 body parts on the partner animal.  
889 This can be done with any annotation software; we used a modified version of the free ‘DeepPoseKit-Anno-  
890 tator’<sup>8</sup> (<https://github.com/jgraving/DeepPoseKit-Annotator/>) included in the supplementary code. This soft-  
891 ware allows easy labeling of the necessary points, and pre-packages training data for use in our training pipe-  
892 line. Body parts are indexed by i/p for implanted/partner animal (‘nose\_p’ is the nose of the partner animal,  
893 for example). Target maps were generated by adding a Gaussian function ( $\sigma = 3$  px for implant,  $\sigma = 1$  px for  
894 other body parts, scaled to peak value = 1) to an array of zeros (at 1/4th the resolution of the input color image)  
895 at the location of every labeled body key-point. 1D part affinity maps were created by connecting labeled key-  
896 points in an array of zeros with a 1 px wide line (clipped to max value = 1), and blurring the resulting image  
897 with a Gaussian filter ( $\sigma = 3$  px).

898

899 ***Aligning depth and color data***

900 The camera intrinsics (focal lengths,  $f$ , optical centers,  $p$ , depth scale,  $d_{scale}$ ) and extrinsics (rotation matrices,  
901  $R$ , translation vectors,  $\bar{t}$ ) for both the color and depth sensors can be accessed over the SDK. Depth and color  
902 images were aligned to each other using a pinhole camera model. For example, the  $z$  coordinate of a single  
903 depth pixel with indices  $(i_c, i_d)$  and 16-bit depth value,  $d_{ij}$ , is given by:

904 
$$z_d = d_{ij} \cdot d_{scale}$$

905 And the  $x$  and  $y$  coordinates are given by:

906 
$$\begin{bmatrix} x_d \\ y_d \end{bmatrix} = \begin{bmatrix} (j_d - p_{x,d}) \cdot z_d / f_{x,d} \\ (i_d - p_{y,d}) \cdot z_d / f_{y,d} \end{bmatrix}$$

907 Using the extrinsics between the depth and color sensors, we can move the coordinate to the reference frame  
908 of the color sensor:

909 
$$\begin{bmatrix} x \\ y \\ z \end{bmatrix}_c = R_{d \rightarrow c} \begin{bmatrix} x \\ y \\ z \end{bmatrix}_d + \bar{t}_{d \rightarrow c}$$

910 Using the focal length and optical center, we can project the pixel onto the color image:

911 
$$\begin{bmatrix} i_c \\ j_c \end{bmatrix} = \begin{bmatrix} f_{y,c} \cdot y_c / z_c + p_{y,c} \\ f_{x,c} \cdot x_c / z_c + p_{x,c} \end{bmatrix}$$

912 For assigning color pixel values to depth pixels, we simply rounded the color pixel indices  $(i_c, i_d)$  to the  
913 nearest integer and cloned the value. More computationally intensive methods based on ray-tracking exist  
914 ('rs2\_project\_color\_pixel\_to\_depth\_pixel' in the Librealsense SDK, for example), but the simple pinhole  
915 camera approximation yielded good results (small jitter average out across multiple key-points) which al-  
916 lowed us to skip the substantial computational overhead of ray tracing for our data pre-processing.

917

918 ***3D calibration and alignment***

919 To align the cameras in space, we first mounted a blue ping-pong ball on a stick and moved it around the  
920 behavioral arena while recording both color and depth video. For each camera, we used a combination of

921 motion filtering, color filtering, smoothing and thresholding to detect the location of the ping-pong ball in the  
922 color frame (details in code). We then aligned the color frames to depth frames and extracted the correspond-  
923 ing depth pixels, yielding a partial 3D surface of the ping-pong ball. By fitting a sphere to this partial surface,  
924 we could estimate the 3D coordinate of the center of the ping-pong ball (**Fig. 3a**). This procedure yielded a  
925 3D trajectory of the ping-pong ball in the reference frame of each camera (**Fig. 3b**). We used a robust regres-  
926 sion method (RANSAC routines to fit a sphere with a fixed radius of 40 mm, modified from routines in  
927 <https://github.com/daavoo/pyntcloud>), insensitive to errors in the calibration ball trajectory to estimate the  
928 transformation matrices needed to bring all trajectories into the same frame of reference (**Fig. 3c**).

929

### 930 *Body model*

931 We model each mouse at two prolate ellipsoids. The model is specified by the 3D coordinate of the center of  
932 the hip ellipsoid,  $\bar{c}_{hip} = [x, y, z]$ , and the major and minor axis of the ellipsoids are scaled by a coordinate,  
933  $s \in [0,1]$  that can morph the ellipsoid from long and narrow to short and fat:

$$934 \quad a_{hip} = a_{hip,0} + a_{hip,\Delta} \cdot s$$

$$935 \quad b_{hip} = b_{hip,0} + b_{hip,\Delta} \cdot (1 - s)$$

936 The ‘neck’ (the joint of rotation between the hip and nose ellipsoid) is sitting a distance,  $d_{hip} = 0.75 \cdot a_{hip}$ ,  
937 along the central axis of the hip ellipsoid. In the frame of reference of the mouse body (taking  $\bar{c}_{hip}$  as the  
938 origin, with the major axis of the hip ellipsoid along the  $x$ -axis), a unit vector pointing to of the nose ellipsoid,  
939 from the ‘neck’ to the center of the nose ellipsoid along it’s major axis is:

$$940 \quad \bar{e}_{nose} = \begin{bmatrix} \cos \theta \\ \sin \theta \cos \phi \\ \sin \theta \sin \phi \end{bmatrix}$$

941 In the frame of reference of the laboratory (‘world coordinates’), we allow the hip ellipsoid to rotate around  
942 the  $z$ -axis (‘left’/‘right’) and around the  $y$ -axis (‘up’/‘down’, in the frame of reference of the mouse). We

943 define  $\mathbf{R}(\alpha_x, \alpha_y, \alpha_z)$  as a 3D rotation matrix specifying the rotation by an angle  $\alpha$  around the three axes, and  
 944  $\mathbf{R}(\bar{v}_1, \bar{v}_2)$  as a 3D rotation matrix that rotates the vector  $\bar{v}_1$  onto  $\bar{v}_2$ . The we can define:

$$945 \quad \mathbf{R}_{hip} = \mathbf{R}(0, \beta, \gamma)$$

$$946 \quad \mathbf{R}_{head} = \mathbf{R}(\bar{e}_x, \bar{e}_{nose})$$

947 , where  $\bar{e}_x$  is a unit vector along the  $x$ -axis. In the frame of reference of the mouse body, the center of the nose  
 948 ellipsoid is:

$$949 \quad \bar{c}_{nose,mouse} = \mathbf{R}_{head} \begin{bmatrix} d_{nose} \\ 0 \\ 0 \end{bmatrix} + \begin{bmatrix} d_{hip} \\ 0 \\ 0 \end{bmatrix}$$

950 So, in world coordinates, the center is:

$$951 \quad \bar{c}_{nose,world} = \mathbf{R}_{hip} \bar{c}_{nose,mouse} + \bar{c}_{hip}$$

952 The center of the neural implant is offset from the center of the nose ellipsoid by a distance  $x_{impl}$  along the  
 953 major axis of the nose ellipsoid, and a distance  $z_{impl}$  orthogonal to the major axis. We allow the implant to  
 954 rotate around the nose ellipsoid by an angle,  $\psi$ . Thus, in the frame of reference of the mouse body, the center  
 955 of the ellipsoid is:

$$956 \quad \bar{c}_{impl,mouse} = \mathbf{R}_{head} \begin{bmatrix} s_{impl} \\ d_{impl} \cdot \cos \psi \\ d_{impl} \cdot \sin \psi \end{bmatrix} + \begin{bmatrix} d_{hip} \\ 0 \\ 0 \end{bmatrix}$$

957 And in world coordinates, same as the center of the nose ellipsoid:

$$958 \quad \bar{c}_{impl,world} = \mathbf{R}_{hip} \bar{c}_{impl,mouse} + \bar{c}_{hip}$$

959 We calculated other skeleton points (tip of the nose ellipsoid, etc.) in a similar method. We can use the rotation  
 960 matrices for the hip and the nose ellipsoids to calculate the characteristic ellipsoid matrices:

$$961 \quad \mathbf{Q}_{hip} = \mathbf{R}_{hip} \begin{bmatrix} 1/a_{hip}^2 & 0 & 0 \\ 0 & 1/b_{hip}^2 & 0 \\ 0 & 0 & 1/b_{hip}^2 \end{bmatrix} (\mathbf{R}_{hip})^T$$

$$962 \quad \mathbf{Q}_{nose} = \mathbf{R}_{hip} \mathbf{R}_{head} \begin{bmatrix} 1/a_{nose}^2 & 0 & 0 \\ 0 & 1/b_{nose}^2 & 0 \\ 0 & 0 & 1/b_{nose}^2 \end{bmatrix} (\mathbf{R}_{hip} \mathbf{R}_{head})^T$$

963 Calculating the shortest distance from a point to the surface of an 3D ellipsoid in 3 dimensions requires solving  
 964 a computationally-expensive polynomial<sup>19</sup>. Doing this for each of the thousands of points in the point-cloud,  
 965 multiplied by four body ellipsoids, multiplied by 200 particles pr. fitting step is not computationally tractable.  
 966 Instead, we use the shortest distance to the surface,  $\tilde{d}$ , along a path that passes through the centroid (Supple-  
 967 mentary Fig. 4a-b). This is a good approximation to  $d$  (especially when averaged over many points), and the  
 968 calculation of  $\tilde{d}$  can be implemented as pure vectorized linear algebra, which can be calculated very effi-  
 969 ciently on GPU<sup>20</sup>. Specifically, to calculate the distance from any point  $\bar{p}$  in the point-cloud, we just center  
 970 the points on the center of an ellipsoid, and – for example – calculate:

$$971 \quad \bar{p}' = \bar{p} - \bar{c}_{hip}$$

$$972 \quad \tilde{d} = \left| 1 - \|\bar{p}'\|_{Q_{hip}}^{-1} \right| \cdot \|\bar{p}'\| \quad \text{where} \quad \|\bar{p}'\|_{Q_{hip}} = \sqrt{\langle \bar{p}', \bar{p}' \rangle_{Q_{hip}}} = \sqrt{(\bar{p}')^T Q_{hip} \bar{p}'}$$

973 In fitting the model, we used the following constants.

974

### 975 ***Loss function evaluation and tracking***

976 Joint position of the two mice is represented as a particle in 17-dimensional space. For each data frame, we  
 977 start with a proposal particle (leftmost green block, based on previous frames), from which we generate 200  
 978 particles by pseudo-random perturbation within a search space (next green block). For each proposal particle,  
 979 we calculate three types of weighted loss contributions: loss associated with the distance from the point-cloud  
 980 to the surface of the mouse body models (top path, green color), loss associated with body key-points (middle  
 981 path, key-point colors as in and loss associated with overlap of the two mouse body models (bottom path,  
 982 purple color). We broadcast the results in a way, which allows us to consider all  $200 \times 200 = 40.000$  possible  
 983 joint postures of the two mice. After calculation, we pick the top 200 joint postures with the lowest overall

984 loss, and anneal the search space, or – if converged – continue to the next frame. When we continue to a new  
 985 frame, we add the fitted frame to a KRLS-T filter bank (online adaptive filter for prediction), which proposes  
 986 the next position of the particle for the next frame, based on previous frame. All loss function calculations,  
 987 and KRLS-T predictions as pure tensor algebra, that can be fully vectorized and executed on a GPU.

988

### 989 *State space filtering of raw tracking data*

990 After tracking, the coordinates of the skeleton points ( $c_{hip}$ ,  $c_{nose}$ , etc.) were smoothed with a 3D kinematic  
 991 Kalman filter tracking both the 3D position ( $p$ ), velocity ( $v$ ) and (constant) acceleration ( $a$ ). For example, for  
 992 the center of the hip coordinate:

$$993 \quad \bar{x} = [p_x, v_x, a_x, p_y, v_y, a_y, p_z, v_z, a_z]$$

$$994 \quad \bar{z} = [c_{hip,x}, c_{hip,y}, c_{hip,z}]$$

$$995 \quad \mathbf{F} = \begin{bmatrix} \mathbf{F}' & \mathbf{0} & \mathbf{0} \\ \mathbf{0} & \mathbf{F}' & \mathbf{0} \\ \mathbf{0} & \mathbf{0} & \mathbf{F}' \end{bmatrix}, \text{ where } \mathbf{F}' = \begin{bmatrix} 1 & dt & \frac{1}{2}dt^2 \\ 0 & 1 & dt \\ 0 & 0 & 1 \end{bmatrix}$$

$$996 \quad \mathbf{H} = \begin{bmatrix} 1 & 0 & 0 & 0 & 0 & 0 & 0 & 0 & 0 \\ 0 & 0 & 0 & 1 & 0 & 0 & 0 & 0 & 0 \\ 0 & 0 & 0 & 0 & 0 & 0 & 1 & 0 & 0 \end{bmatrix}$$

$$997 \quad \mathbf{P} = \mathbf{1}_{9 \times 9} \cdot \sigma_{cov}^2$$

$$998 \quad \mathbf{R} = \mathbf{I}_{3 \times 3} \cdot \sigma_{measurement}^2$$

$$999 \quad \mathbf{Q} = \begin{bmatrix} \mathbf{Q}' & \mathbf{0} & \mathbf{0} \\ \mathbf{0} & \mathbf{Q}' & \mathbf{0} \\ \mathbf{0} & \mathbf{0} & \mathbf{Q}' \end{bmatrix} \cdot \sigma_{process}^2$$

1000 where  $\mathbf{Q}'$  is the Q matrix for a discrete constant white noise model  $\mathbf{Q}' = \begin{bmatrix} \frac{1}{4}dt^4 & \frac{1}{2}dt^3 & \frac{1}{2}dt^2 \\ \frac{1}{2}dt^3 & dt^2 & dt \\ \frac{1}{2}dt^2 & dt & 1 \end{bmatrix}$  and

1001  $\sigma_{measurement} = 0.015$  m,  $\sigma_{process} = 0.01$  m,  $\sigma_{cov}^2 = 0.0011$  m<sup>2</sup>. The  $\sigma$ 's were the same for all points, ex-  
 1002 cept the slightly more noisy estimate of the center of the implant, where we used.  $\sigma_{measurement} =$



1003 0.02 m,  $\sigma_{process} = 0.01$  m,  $\sigma_{cov}^2 = 0.0011$  m<sup>2</sup> From the frame rate (60 fps),  $dt = \frac{1}{60}$  s. The maximum-like-  
1004 lihood trajectory was estimated with the Rauch-Tung-Striebel method<sup>30</sup> with a fixed lag of 16 frames. The  
1005 filter and smoother was implemented using the ‘filterpy’ package (<https://github.com/rlabbe/filterpy>). The  
1006 spine scaling,  $s$ , was smoothed with a similar filter in 1D, except that we did not model acceleration, only  $s$   
1007 and a (constant)  $s$  ‘velocity’, with  $\sigma_{measurement} = 0.3$ ,  $\sigma_{process} = 0.05$  m,  $\sigma_{cov}^2 = 0.0011$ .  
1008 After filtering the trajectories of the skeleton points, we recalculated the 3D rotation matrices of the hip and  
1009 head ellipsoid by the vectors pointing from  $c_{hip}$  to  $c_{mid}$  (from the middle of the hip ellipsoid to the neck joint),  
1010 and from  $c_{hip}$  to  $c_{nose}$  (from the neck joint to the middle of the nose ellipsoid). We then converted the 3D  
1011 rotation matrixes to unit quaternions, and smoothed the 3D rotations by smoothing the quaternions with an  
1012 10-frame boxcar filter, essentially averaging the quaternions by finding the largest eigenvalue of a matrix  
1013 composed of the quaternions within the boxcar<sup>32</sup>. After smoothing the ellipsoid rotations, we re-calculated  
1014 the coordinates of the tip of the nose ellipsoid ( $c_{tip}$ ) and the posterior end of the hip ellipsoid ( $c_{tail}$ ) from the  
1015 smoothed central coordinates, rotations, and – for  $c_{tail}$  – the smoothed spine scaling. A walkthrough of the  
1016 state space filtering pipeline is shown in **Supplementary Fig. 6**.

1017

### 1018 ***Template matching***

1019 To detect social events, we calculated three social distances, from three instantaneous ‘social distances’, de-  
1020 fined as the 3D distance between the tip of each animal’s noses (‘nose-to-nose’), and from the tip of each  
1021 animal’s nose to the posterior end of the conspecific’s hip ellipsoid (‘nose-to-tail’; Fig. 6c). From these social  
1022 distances, we could automatically detect when the mouse bodies were in a nose-to-nose (if the nose-to-nose  
1023 distance was  $< 2$  cm and the nose-to-tail distance was  $> 6$  cm) and in a nose-to-tail configuration (if the nose-  
1024 to-nose distance was  $> 6$  cm and the nose-to-tail distance was  $> 2$  cm). The events were detected by the logic  
1025 conditions, and then single threshold crossings due to noise were removed by binary opening with a 3-frame  
1026 kernel, followed by binary closing with a 30-frame kernel.

1027

## 1028 *State space modeling of mouse behavior*

1029 State space modeling of the locomotion behavior was performed in Pyro<sup>35</sup> a GPU-accelerated probabilistic  
1030 programming language built on top of Pytorch<sup>25</sup>. We modeled the (centered and whitened) locomotion be-  
1031 havior as a hidden Markov model with discrete latent states,  $z$ , and associated transition matrix,  $\mathbf{T}$ .

$$1032 \quad z(t + 1) = \text{Categorical}(e^{z(t)} \cdot \mathbf{T})$$

$$1033 \quad \mathbf{T} = \begin{bmatrix} p_{ij} & \cdots \\ \vdots & \ddots \end{bmatrix}$$

1034 To make the model ‘sticky’ (discourage fast switching between latent states) we draw the transition probabil-  
1035 ities,  $p_{ij}$  from a Dirichlet prior with a high mass near the ‘edges’ and initialize  $\mathbf{T}_{init} = (1 - \eta)\mathbf{I} + \eta/n_{states}$   
1036 where  $\eta = 0.05$ .

$$1037 \quad p \sim \text{Diriclet}(0.5)$$

1038 Each state emits a forward speed and a left speed, drawn from a two-dimensional gaussian distribution with  
1039 a full covariance matrix.

$$1040 \quad \begin{bmatrix} v_{\text{fwd}} \\ v_{\text{left}} \end{bmatrix} \sim \text{MVNormal}(\mu, \mathbf{S})$$

1041 We draw the mean of the states from a normal distribution and use a LKJ Cholesky prior for the covariance:

$$1042 \quad \mu \sim \text{Normal}(0,1)$$

$$1043 \quad \mathbf{S} = \begin{bmatrix} \sigma_{\text{fwd}} & 0 \\ 0 & \sigma_{\text{left}} \end{bmatrix} \mathbf{L} \begin{bmatrix} \sigma_{\text{fwd}} & 0 \\ 0 & \sigma_{\text{left}} \end{bmatrix}$$

$$1044 \quad \sigma \sim \text{LogNormal}(-1,1)$$

$$1045 \quad \mathbf{L} \sim \text{LKJcorr}(2)$$

1046 The up speed was modeled in a similar way, except that the latent states were just a one-dimensional normal  
1047 distribution. The means and variances for the latent states was initialized by kmeans clustering of the loco-  
1048 motion speeds. The model was fit in parallel to 600-frame snippets of a subset of the data by stochastic vari-  
1049 ational inference<sup>62</sup>. We used an automatic delta guide function (‘AutoDelta’) and an evidence lower bound

1050 (ELBO) loss function. The model was fitted by stochastic gradient descent with a learning rate of 0.0005.  
1051 After model fitting, we generated the ethograms by assigning latent states by maximum a posteriori probabil-  
1052 ity with a Viterbi algorithm.

1053

### 1054 ***3D head direction estimation***

1055 We use the 3D position of the ear key-points to determine the 3d head direction of the partner animal. We  
1056 assign the ear key-points to a mouse body model by calculating the distance from each key-point to the center  
1057 of the nose ellipsoid of both animals (cutoff: closest to one mouse and  $< 3\text{cm}$  from the center of the head  
1058 ellipsoid, Supplementary Fig 10a). To estimate the 3D head direction, we calculate the unit rejection ( $v_{rej}$ )  
1059 between a unit vector along the nose ellipsoid ( $v_{nose}$ ) and a unit vector from the neck joint ( $c_{mid}$ ) to the  
1060 average 3D position of the ear key-points that are associated with that mouse ( $v_{ear\_direction}$ , Supplementary  
1061 Fig. 10b). If no ear key-points were detected in a frame, we linearly interpolate the average 3D position. To  
1062 average out jitter, the estimates of the average ear coordinates and the center of the nose coordinate were  
1063 smoothed with a Gaussian ( $\sigma = 3$  frames). The final head direction vector was also smoothed with a Gaussian  
1064 ( $\sigma = 10$  frames).

1 **Supplementary material to:**

2 **Automatic tracking of mouse social posture dynamics**

3 **by 3D videography, deep learning and GPU-accelerated robust optimization**

4

5 **Christian L. Ebbesen<sup>1,2,\*</sup> & Robert C. Froemke<sup>1,2,3,\*</sup>**

6

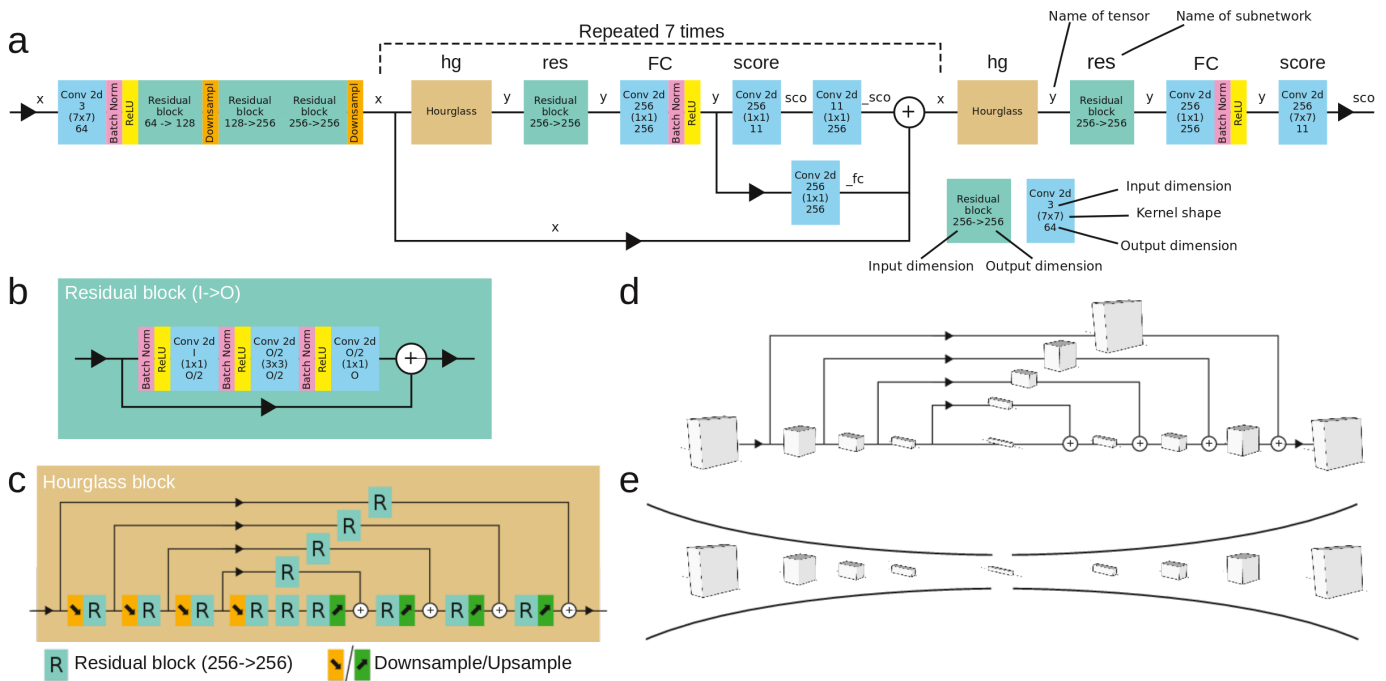
7 <sup>1</sup> Skirball Institute of Biomolecular Medicine, Neuroscience Institute, Departments of Otolaryngology, Neu-  
8 rosence and Physiology, New York University School of Medicine, New York, NY, 10016, USA.

9 <sup>2</sup> Center for Neural Science, New York University, New York, NY, 10003, USA.

10 <sup>3</sup> Howard Hughes Medical Institute Faculty Scholar.

11 \* Correspondence to: C.L.E. ([christian.ebbesen@nyumc.org](mailto:christian.ebbesen@nyumc.org)) or R.C.F. ([robert.froemke@med.nyu.edu](mailto:robert.froemke@med.nyu.edu))

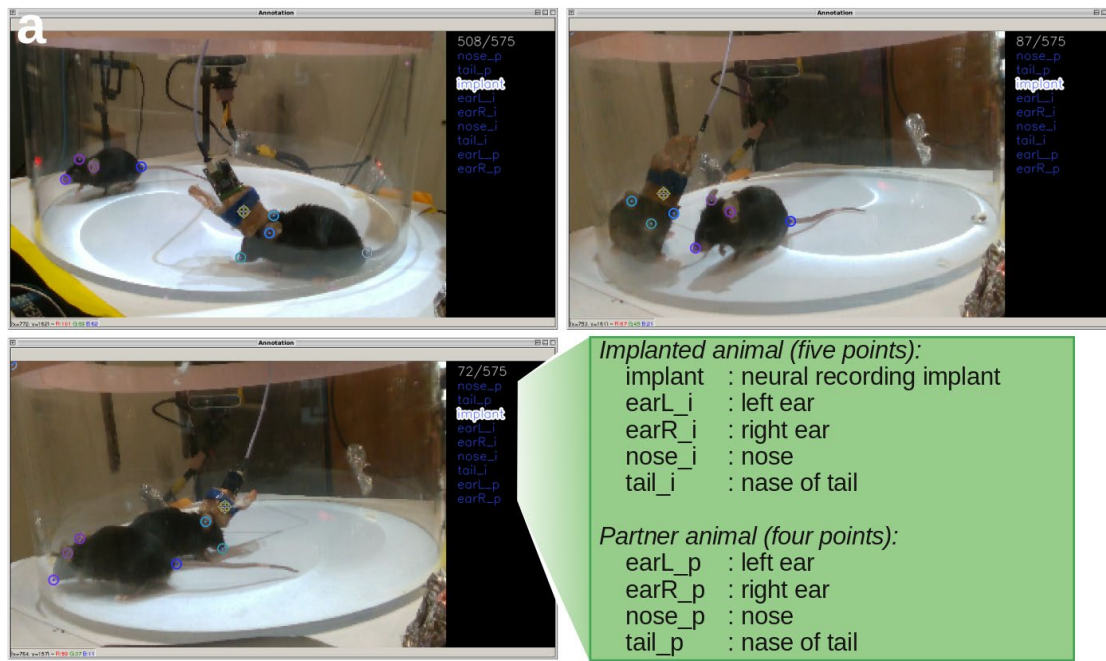
## 12 SUPPLEMENTARY FIGURES



13

14

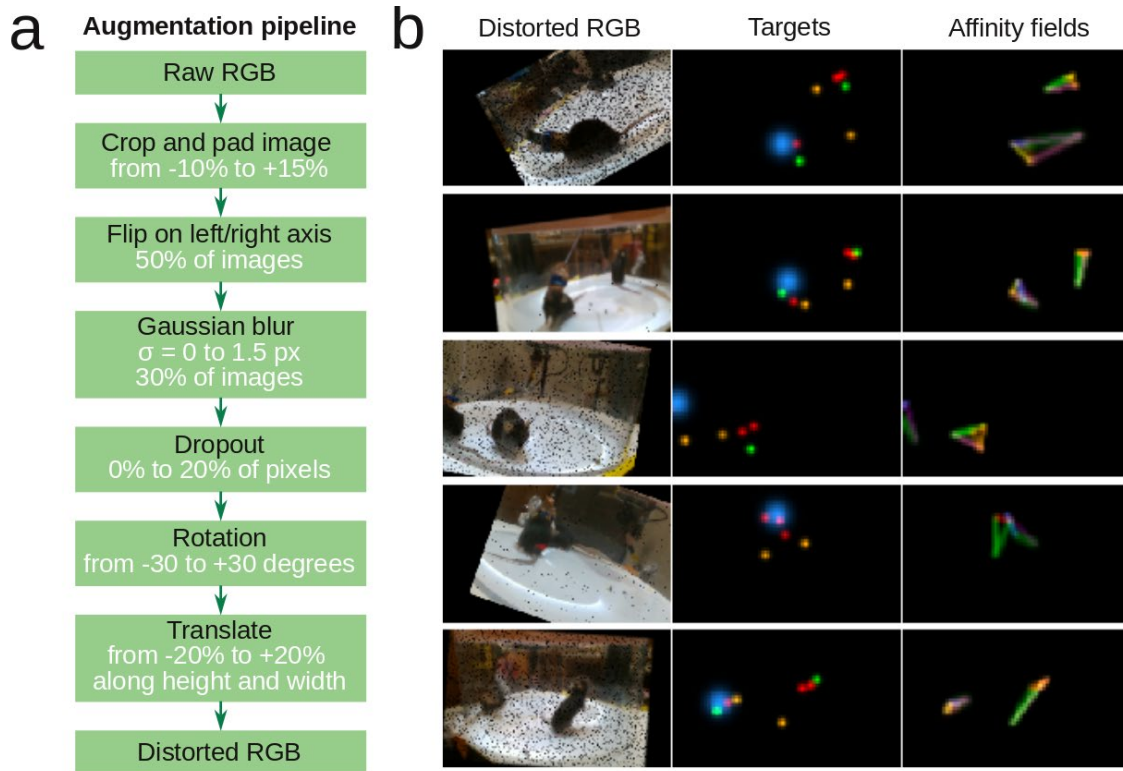
15 **Supplementary Figure 1. Deep convolutional neural network architecture. a**, Schematic of flow of ten-  
 16 sors through deep convolutional neural network. Convolutional blocks show kernel shapes and input/output  
 17 dimensions of feature dimension, starting from 3 (RGB image), expanding to 256 during hourglass blocks,  
 18 and ending in 11 for intermediate and final outputs (4 body point targets, 7 part affinity fields). Full imple-  
 19 mentation details (e.g., including stride, padding, bias, etc.) are included in supplementary code. **b**, Schematic  
 20 of a single residual block. **c**, Schematic of a single hourglass block. Upsampling (green, nearest neighbor) and  
 21 downsampling (orange, by max pooling, both a factor of 2) happens along 2D image space (height/width). **d**,  
 22 Shapes of tensors flowing through hourglass block. Along bottom path, feature dimension stays constant, but  
 23 image dimensions (height/width) are increasingly downsampled, and then upsampled again. After each up-  
 24 sample, tensors are merged with skip connections (paths above). **e**, The hourglass-like shape that gives name  
 25 to the network architecture.



26

27

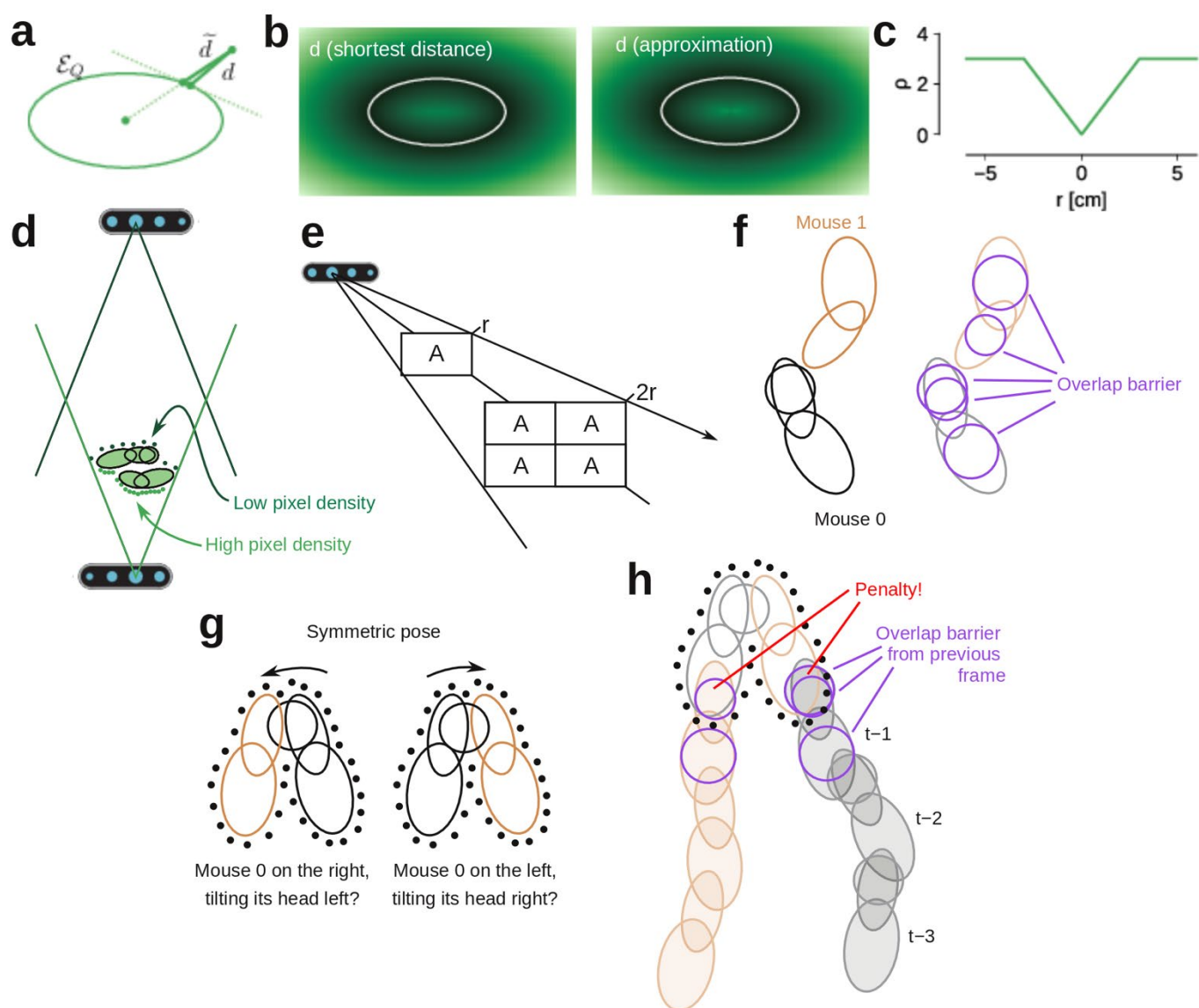
28 **Supplementary Figure 2. GUI for labeling of training data for the neural network. a,** For training the  
29 network to recognize body parts, we must generate labeled frames by manual annotation. For each frame, 1-  
30 5 body parts are labeled on the implanted animal and 1-4 body parts on the partner animal. This can be done  
31 with any annotation software; we used a modified version of the free ‘DeepPoseKit-Annotator’ (Graving et  
32 al., 2019) (<https://github.com/jgraving/DeepPoseKit-Annotator/>) included in the supplementary code. This  
33 software allows easy labeling of the necessary points, and pre-packages training data for use in our training  
34 pipeline. Body parts are indexed by i/p for implanted/partner animal (‘nose\_p’ is the nose of the partner animal,  
35 for example).



36

37

38 **Supplementary Figure 3. Augmentation pipeline for network training.** **a**, Flowchart of augmentation  
39 pipeline used to generate distorted frames during network training. **b**, Examples of distorted labeling frames  
40 generated by augmentation pipeline, as well as corresponding body part targets and affinity fields used during  
41 training.



42

43 **Supplementary Figure 4. Loss function calculation details.** **a**, Shortest distance to surface of an ellipsoid,

44  $d$ , and our approximation,  $\tilde{d}$ . **b**,  $\tilde{d}$  is a good approximation to  $d$ . Color map, value of  $d/\tilde{d}$ . White line, ellip-

45 soid surface. **c**, The loss function,  $\rho$ , associated with the pointcloud is the mean absolute error of the distance

46 estimate, truncated at  $\pm 3.0$  cm **d**, Pixel density of the point-cloud depends on distance to the fixed-resolution

47 depth cameras. **e**, Pixel density is inversely proportional to the square of the distance to depth camera. **f**,

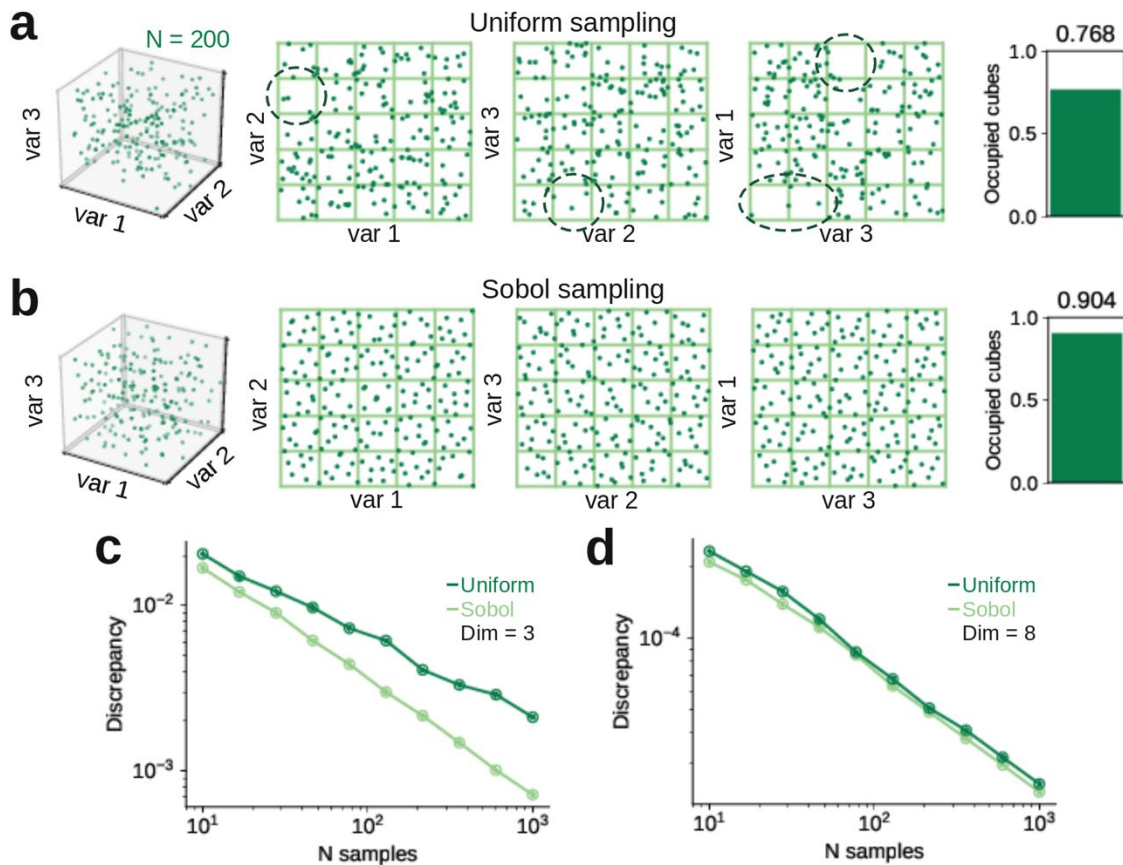
48 Overlap barrier spheres (implant sphere and spheres centered on the body ellipsoids with a radius equal to the

49 minor axis). **g**, Example of mirror symmetric body position (side-by-side, facing same direction), resulting in

50 ambiguity in animal identity if only one frame is considered. **h**, To include the context of previous frames, we

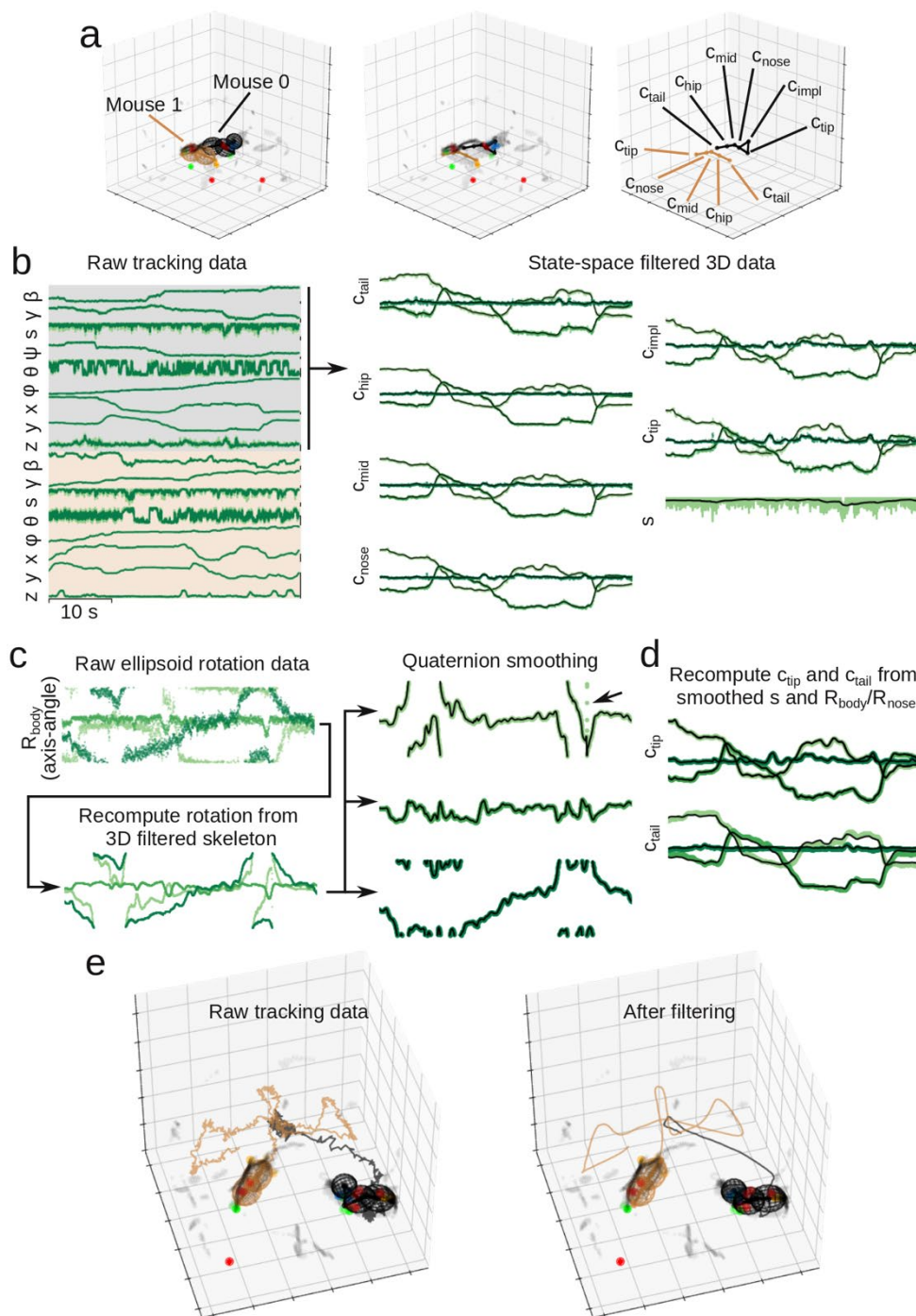


51 add an overlap loss penalty (similar to **f**) between each mouse and the position of the interaction partner in  
52 the previous frame. In panel **g**, right, we would add a penalty term to the particle representing joint body pose.  
53 In contrast, in panel **g**, left, this penalty is zero as there is no overlap with the position of the conspecific in  
54 the previous frame.



55

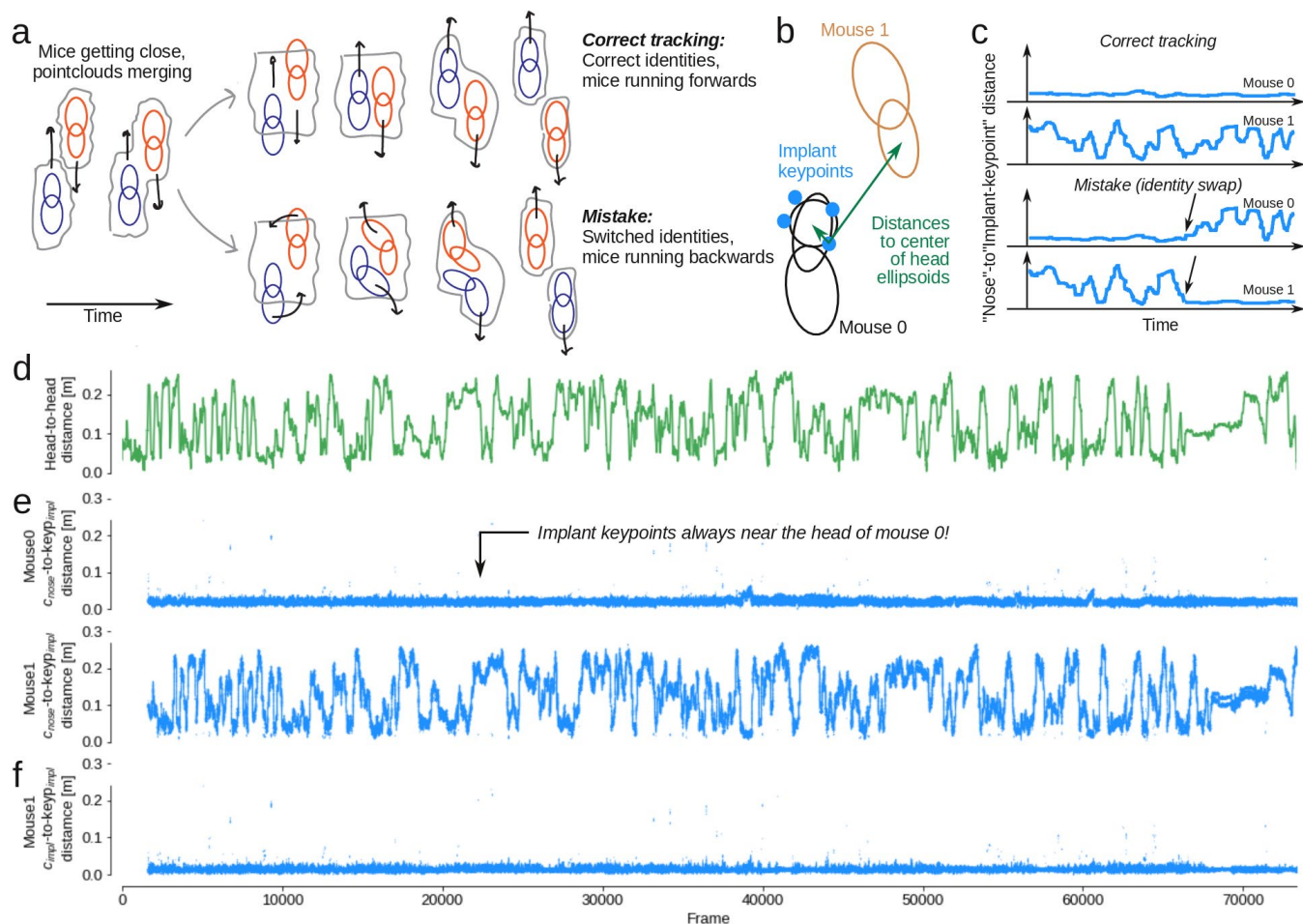
56 **Supplementary Figure 5. Quasi-random particle filter exploration strategy.** **a**, Left, 3D plot. Middle, 2D  
57 projection plots of three random variables, drawn from independent uniform distributions. Points in 3D space  
58 do not fill space well; in the 2D projections, there are squares (i.e., full rows, columns and pipes) of the 3D  
59 space not sampled at all (dashed lines). Right, partitioning space in 20%-cubes (green lines), only 76.8 % of  
60 cubes are occupied. **b**, Same as **a**, but variables are drawn from quasi-random Sobol sequence (Sobol, 1967).  
61 Points are more evenly dispersed in space, and 90.4% of all 20%-cubes are sampled. **c**, Mean discrepancy as  
62 function of sample number, for 3-dimensional (like panels **a,b**) uniform random sequence and a Sobol se-  
63 quence, calculated across 100 random sequences. The Sobol sequences have a lower discrepancy, i.e. sample  
64 more regions of space. **d**, Same as **c**, but for 17-dimensional variables (like our joint body posture particles).



65

66 **Supplementary Figure 6. State space filtering of tracked body models.** **a**, Estimated 3D locations of body  
 67 model surfaces (wireframes, left) and skeletons (dots and lines, right) for an example frame. **b**, Fitted joint  
 68 pose parameters for the two mouse body models (left, 100 s snippet) and corresponding 3D coordinates of the  
 69 body skeleton points, and the spine scaling,  $s$ , for the implanted mouse (right, same 100 s). **c**, Raw 3D rotation  
 70 angle of the nose ellipsoid of the implanted animal (axis-angle representation), recalculated 3D rotation angles

71 from the filtered skeleton points, and final 3D rotation angles after quaternion smoothing (note the smoothing  
72 our of noise, indicated by arrow). **d**, Recalculated  $c\_nose$  and  $c\_tail$  from the smoothed 3D rotations and  
73 smoothed spine scaling. **e**, Example frame before (left) and after state space filtering of the tracked data (right).



74

75 **Supplementary Figure 7. Implant-to-nose distance demonstrates that there are no swapped identities.**

76 **a**, Schematic showing two common errors in tracking algorithms: Swapped identities and swapped directions.

77 When the mice approach each other, their point clouds will merge. Because resolution and frame rates are

78 limited, it can be hard to estimate body postures in this configuration. For example, if the tracking algorithm

79 is not properly spatiotemporally regularized, the algorithm might mistakenly swap mouse identities, such that

80 the mice appear to be running backwards (shown in bottom row). Direction swaps and identity swaps can also

81 happen independently. For example, when mice are allogrooming, or passing over/under each other, identities

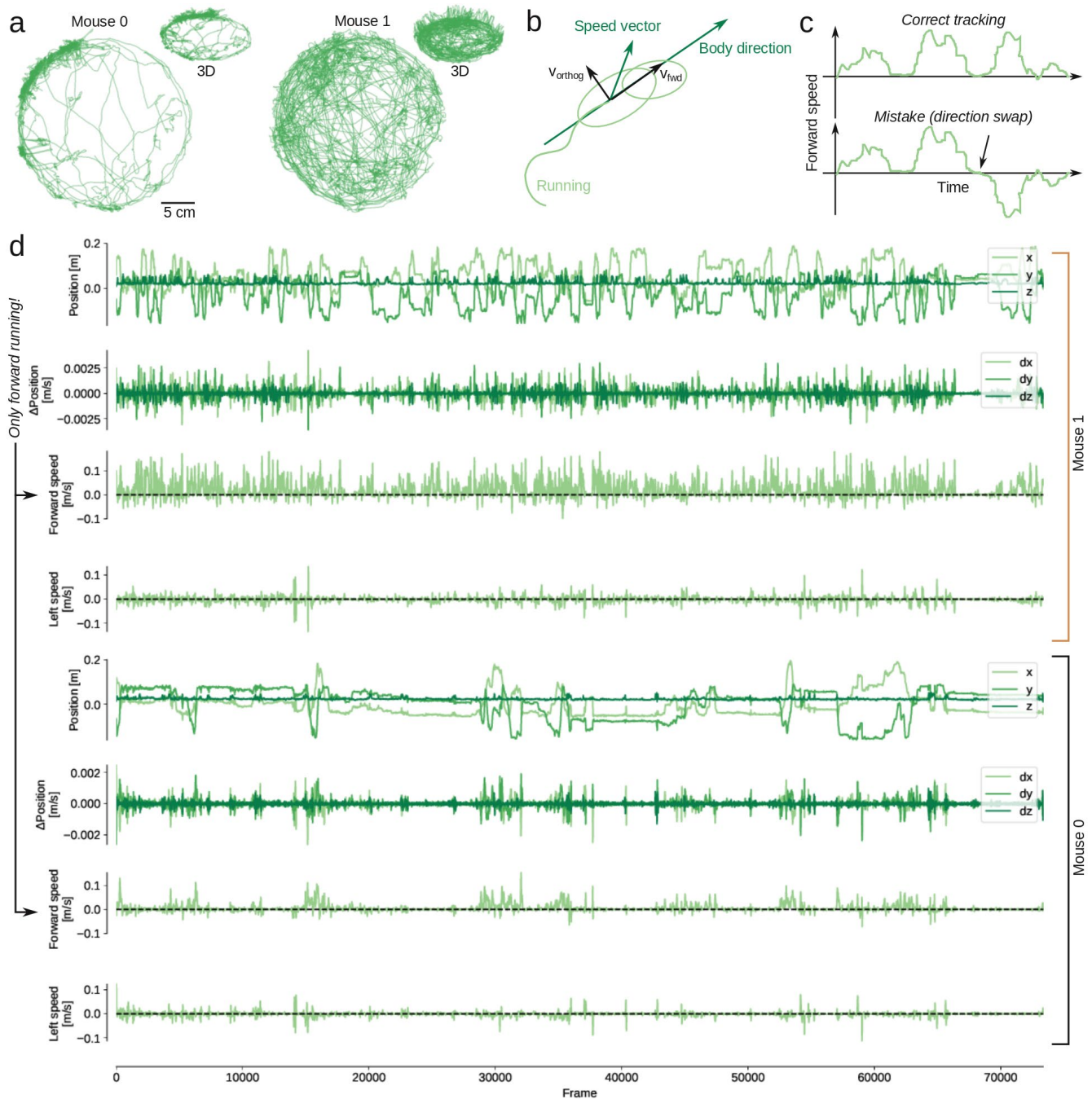
82 might swap, but both mice can still appear to run normally with no apparent errors. Conversely, when a mouse

83 is self-grooming, their point-cloud essentially resembles a ball, and when they start moving again, it may not

84 be clear if they are 'really' moving forward or backwards. **b**, For all frames, we calculated the distance be-

85 tween implant key-points and the centroid of both nose ellipsoids. **c**, If there is an identity swap of the mice,

86 this is will be evident in the distance between the implant key-points and the head of both mice. In correct  
87 tracking (top row), implant body model always follows the same mouse. In tracking with mistakes (bottom  
88 row), implant will switch from being close to one mouse, to being close to the other mouse. **d**, The head-to-  
89 head (nose-centroid-to-nose-centroid) distance for the two mice, across the session. The mice often closely  
90 interact (low head-to-head distance), allowing for potential identity swaps. **e**, Distance between implant key-  
91 points and the nose centroid for both mice, across the session. The implant key-points are always near mouse0  
92 and there are no identity swaps. **f**, The actual implant-key-point to implant-skeleton-point distance for mouse  
93 0, across the session, is lower than the distance to the centroid of the nose ellipsoid.

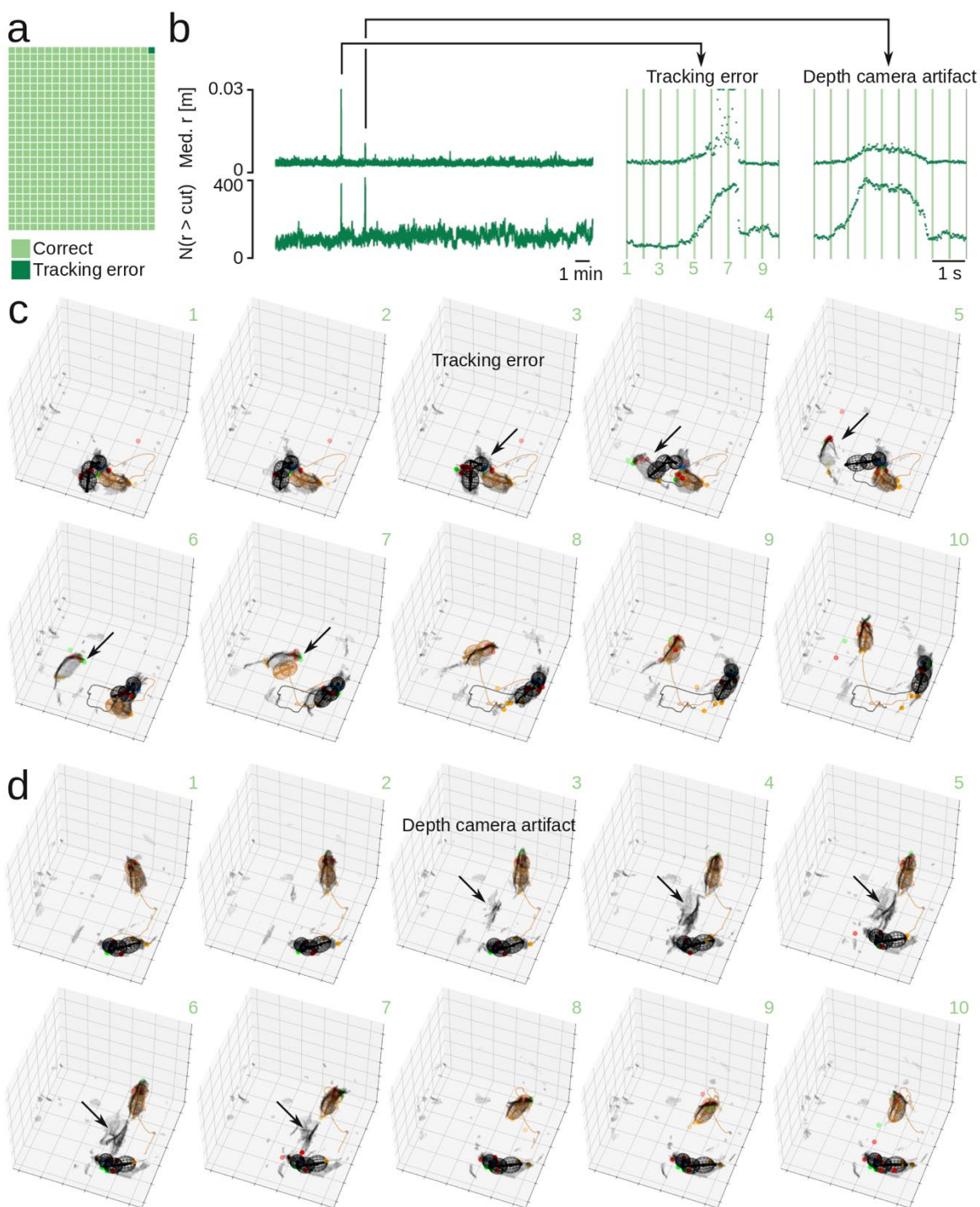


94

95 **Supplementary Figure 8. Calculation of movement speed in egocentric coordinates.** **a**, Running behav-  
96 ior of the two mice (centroid of the hip ellipsoid) across the behavioral session, shown in 2D (top-down  
97 view) and 3D. **b**, Running speed decomposed into two components, 'forward speed' ( $v_{fwd}$ , projected onto  
98 the orientation of the hip ellipsoid) and 'left speed' ( $v_{orthog}$ , the orthogonal component). **c**, In correct  
99 tracking (top row), running bouts will have positive forward speed. If there is a mistake in the tracking (bot-  
100 tom row), such that the mouse body model has switched direction, the mouse will appear to be 'running

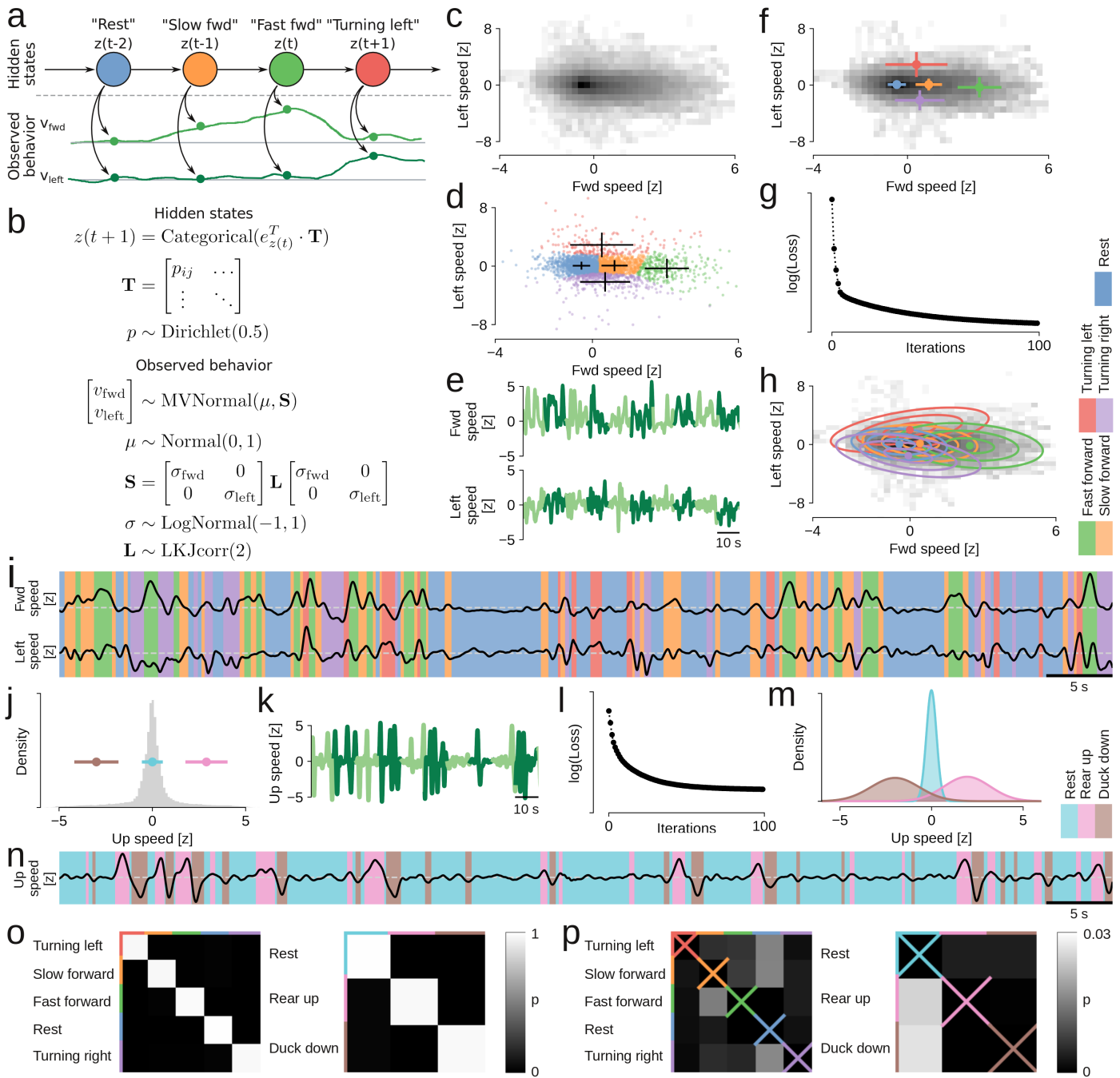
101 backwards'. **d**, Top to bottom: The x,y,z-coordinates of the position (c\_hip) of the mouse at each tracked  
102 frame, the change in position between frames, the forward speed, and the left speed. The four rows are re-  
103 peated for both mice. There are no direction swap mistakes, and across the whole session, both mice only  
104 displayed bouts of forward running (confirmed by visual inspection of raw video).





105  
106 **Supplementary Figure 9. Manual error checking.** **a**, By manual inspection of 500 frames, we detected one  
107 tracking error. **b**, Median point-cloud residual (top) and number of point-cloud points with a residual larger  
108 than the cutoff (bottom, cut = 0.03 m) across an example 21 min recording. These traces show two anomalies:  
109 One tracking error (around frame 17000, the error we also detected by manual inspection of the 500 frames)  
110 and one depth camera artifact (tracking was fine, but a ghostly artifact showed up in the point-cloud for few

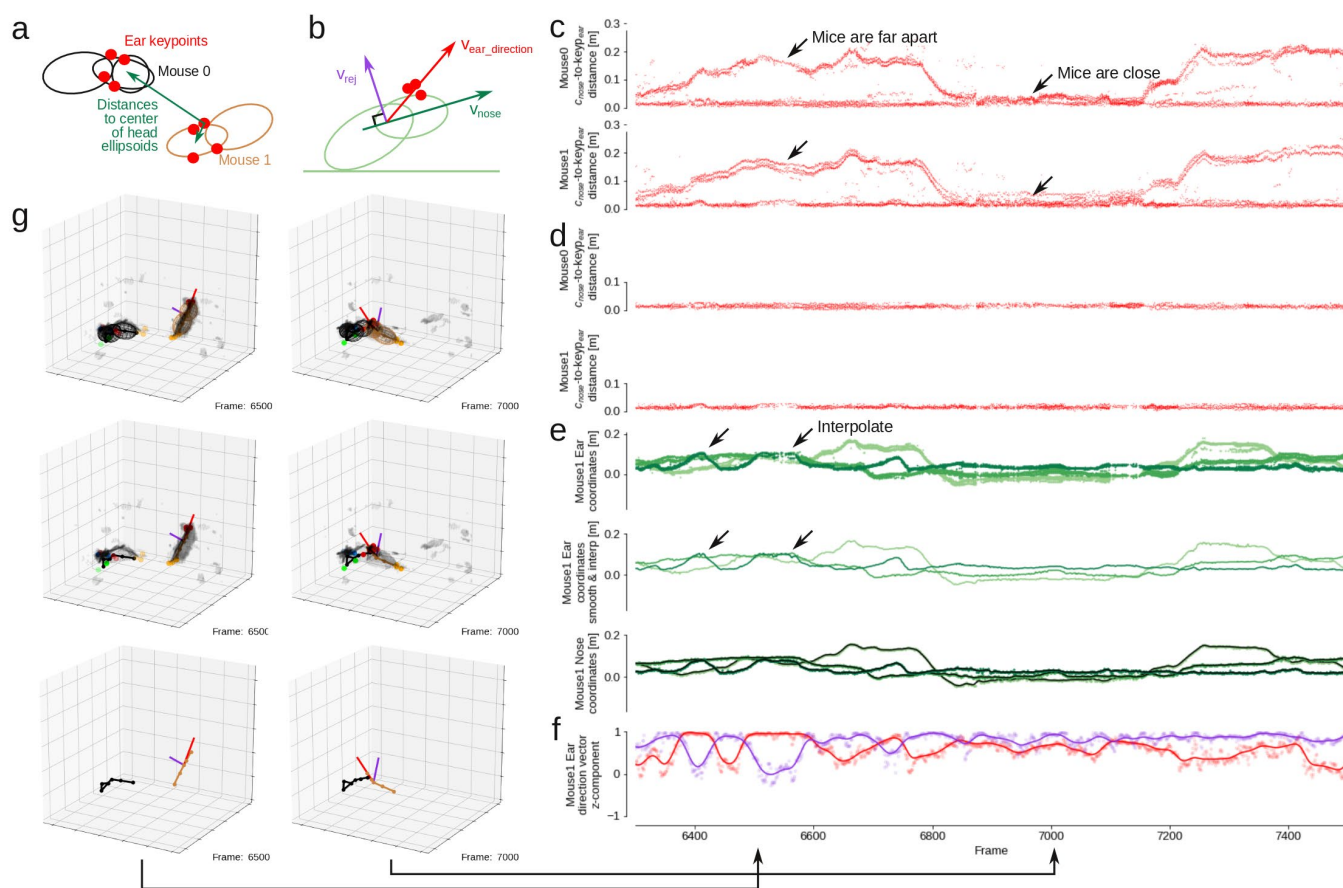
111 a seconds. Due to the of the robust loss function, tracking was not distorted by the artifact). **c**, Ten example  
112 frames showing the tracking error (0.5 s between frames, indicated by vertical lines in panel b). Note that  
113 after the error, the particle filter quickly recovers to correct tracking again. **d**, Ten example frames showing  
114 the depth camera artifact.



115

116 **Supplementary Figure 10. Bayesian modeling and automatic classification of behavioral states.** a, Gen-  
117 erative model fit to the running behavior to automatically classify behavioral states. The model is a hidden  
118 Markov model with discrete latent states (circles), and each state emits a forward speed and a left speed,  
119 drawn from a two-dimensional gaussian distribution with a full covariance matrix. b, The generative model  
120 expressed as equations, showing Bayesian priors for estimating the parameters. c, Joint distribution (on a log-  
121 scale) of the forward speed and left speed, for both mice, across an entire behavioral session. d, Initial position

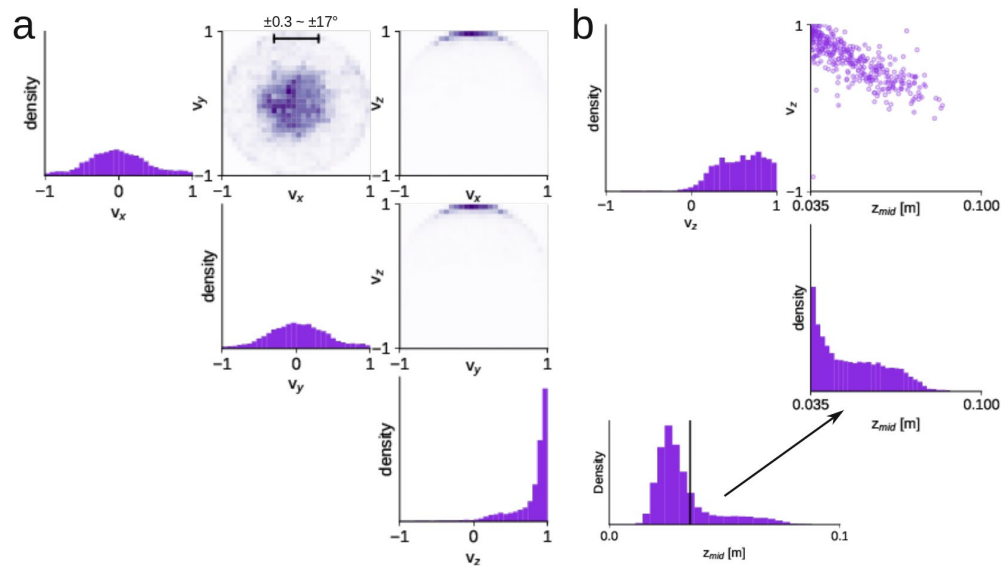
122 for the variation inference, for the model of forward and left speed. Crosses, cluster centers and standard  
123 deviations (calculated independently for fwd/left speed) for clusters assigned by k-means clustering into 5  
124 clusters. Dots, individual samples of fwd/left speed (colors indicate clusters, every 50<sup>th</sup> sample is show). **e**,  
125 Bayesian model was fitted to a subset of the data (5 mins), split and run in parallel on 10-s sequences. The  
126 plot shows example 10-s sequences. **f**, Joint distribution (on a log-scale) of the forward speed and left speed,  
127 for the training data, overlaid with the cluster centers and standard deviations from all data (i.e., from **d**).  
128 Training data cover same velocity space as the whole session (compare with **a**). **g**, Convergence plot showing  
129 the decrease in model loss (increased evidence lower bound) across iterations for the training data. **h**, Loca-  
130 tions and covariance ellipsoids (indicating three standard deviations) for the gaussian emission distributions  
131 associated with the five latent states, after model fitting. The five clusters are easily interpretable, and the  
132 labels are shown on the right. **j**, Initial position for the variation inference for the up speed. Distribution of the  
133 up speed (grey bars), as well as the center and standard deviation of three clusters (colored bars and dots),  
134 assigned by k-means clustering. **i**, Automatically assigned states (by maximum a posterior probability) to an  
135 example sequence of forward and left speed. **k,l,m,n**, same as **e,g,h,i**, but for the model fitting of the emission  
136 gaussians (in one dimension) of the up speed. **o**, Transition probabilities between latent states, for both for-  
137 ward/left speed and up speed models. The sample rate is 60 frames/s, so – since behavioral states are longer  
138 than that – the self-transition probabilities (diagonals) are very high. **p**, As **o**, but without showing the self-  
139 transition probabilities (the diagonals, crossed out). These matrices have understandable structure. For exam-  
140 ple, in the left matrix, the most likely transition from “rest” is to “slow forward”. From “slow forward”, the  
141 mouse is likely to transition to “turning left”, “fast forward” or “turning right”. It is very unlikely to transition  
142 directly from “fast forward” to “rest” or from “turning left” to “turning right”. From the right matrix, we can  
143 see that it is unlikely to transition directly from “rear up” to “rear down”, it is more probable to have a period  
144 of “rest” in between.



145

146 **Supplementary Figure 11. Estimation of 3D heading direction in the partner animal, part I.** **a**, We use  
 147 the 3D position of the ear keypoints to determine the 3d head direction of the partner animal. We assign the  
 148 ear keypoints to a mouse body model by calculating the distance from each keypoint to the center of the nose  
 149 ellipsoid of both animals. **b**, To estimate the 3D head direction, we calculate the unit rejection ( $v_{rej}$ ) between  
 150 a unit vector along the nose ellipsoid ( $v_{nose}$ ) and a unit vector from the neck joint ( $c_{mid}$ ) to the average  
 151 3D position of the ear keypoints that are associated with that mouse ( $v_{ear\_direction}$ ). **c**, The distance from  
 152 all ear keypoints to the center of the nose ellipsoid, for both mice, for an example portion of the recording  
 153 session. **d**, The distance from ear keypoints to the center of the nose ellipsoid, only showing the keypoints that  
 154 we estimate to be associated with each mouse. **e**, Estimated mean 3D position of the ear keypoints associated  
 155 with the partner animal ('Mouse 1'). Top to bottom: Raw 3D position of all keypoints, mean position using  
 156 linear interpolation, smoothed with a Gaussian kernel ( $\sigma = XX$  frames). **f**, The z-component of  $v_{ear\_di}$   
 157 rection and  $v_{rej}$ . The z-component is high, indicating that the ears are on the dorsal side of the head ellipsoid.

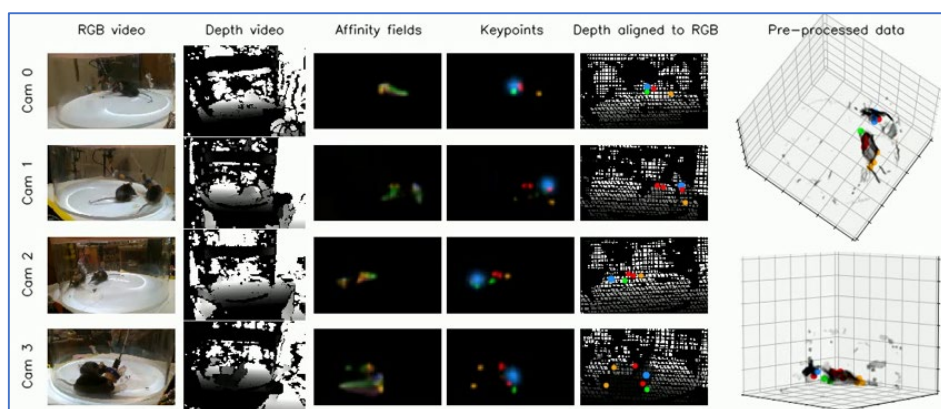
158 When the mouse is running on the ground, both  $v_{\text{ear\_direction}}$  and  $v_{\text{rej}}$  have high z-components (marked  
159 with rightmost arrow), but when the mouse is rearing and tilting the head backwards,  $v_{\text{rej}}$  will be more in  
160 the xy-plane, and have a low z-component (marked with leftmost arrow). **g**, The 3D body positions, of the  
161 frames indicated by arrows in panel **f**.



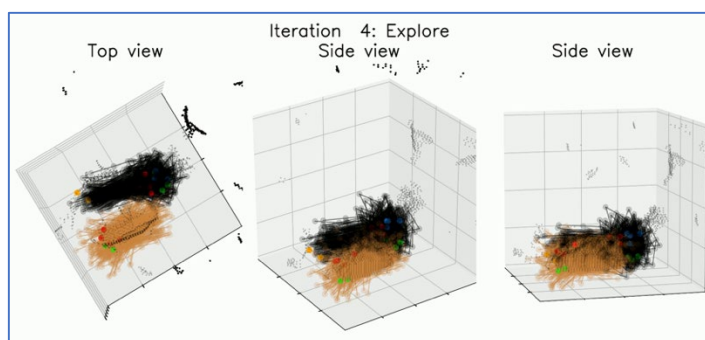
162

163 **Supplementary Figure 12. Estimation of 3D heading direction in the partner animal, part II.** **a**, The joint  
164 distributions of the components of  $v_{rej}$  (Supplementary Fig. 9b) shows that mouse mostly keeps the ears  
165 horizontal, rarely tilting the head more than 17 degrees towards the left or right. As also shown in Supple-  
166 mentary Fig 9f-g, the z-component is mostly close to 1 (pointing straight up), but sometimes smaller, closer  
167 to 0 (meaning that the nose is pointing up towards the sky). **b**, We can dig in to the details of the 3D head  
168 direction behavior. For example, we can decide to only look at the head direction, when the z-coordinate of  
169 the neck ( $z_{mid}$ ) is high (i.e. when the mouse is rearing). Here we find a clear negative correlation between  
170 the z-component of  $v_{rej}$  and  $z_{mid}$ , which matches the visual inspection of the videos: When the mouse  
171 rears up or climbs up against the walls of the transparent social arena, the head tilts back to extend the nose  
172 upwards.

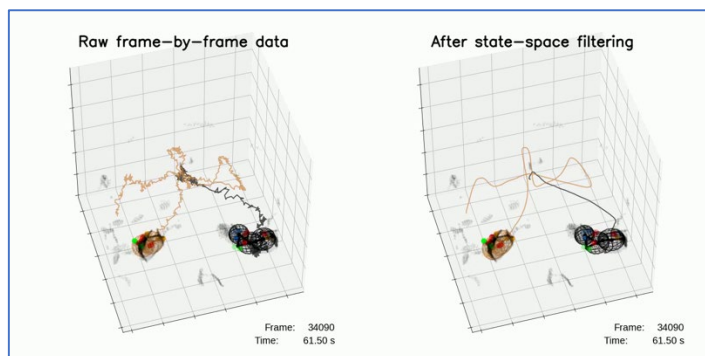
## 173 SUPPLEMENTARY VIDEOS



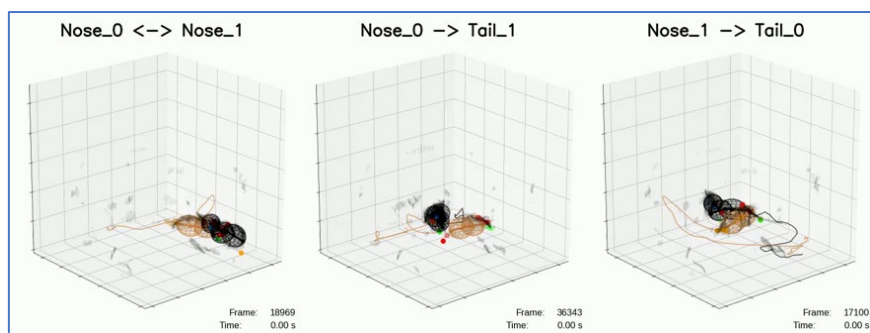
174  
175 **Supplementary Video 1. Pre-processing pipeline.**  
176



177  
178 **Supplementary Video 2. Particle filter behavior.**  
179



180  
181 **Supplementary Video 3. State-space filtering.**  
182



183  
184 **Supplementary Video 4. Social events.**